



Published in final edited form as:

Nat Med. 2020 April ; 26(4): 577–588. doi:10.1038/s41591-020-0757-z.

TMEM30A loss-of-function mutations drive lymphomagenesis and confer therapeutically exploitable vulnerability in B-cell lymphoma

A full list of authors and affiliations appears at the end of the article.

Abstract

Transmembrane protein 30A (TMEM30A) maintains the asymmetric distribution of phosphatidylserine, an integral component of the cell membrane and ‘eat-me’ signal recognized by macrophages. Integrative genomic and transcriptomic analysis of diffuse large B-cell lymphoma (DLBCL) from the British Columbia population-based registry uncovered recurrent biallelic *TMEM30A* loss-of-function mutations, which were associated with a favorable outcome and uniquely observed in DLBCL. Using *TMEM30A*-knockout systems, increased accumulation of chemotherapy drugs was observed in *TMEM30A*-knockout cell lines and *TMEM30A*-mutated primary cells, explaining the improved treatment outcome. Furthermore, we found increased tumor-associated macrophages and an enhanced effect of anti-CD47 blockade limiting tumor growth in *TMEM30A*-knockout models. By contrast, we show that TMEM30A loss-of-function increases B-cell signaling following antigen stimulation—a mechanism conferring selective advantage during B-cell lymphoma development. Our data highlight a multifaceted role for TMEM30A in B-cell lymphomagenesis, and characterize intrinsic and extrinsic vulnerabilities of cancer cells that can be therapeutically exploited.

DLBCL is the most common lymphoma subtype worldwide, accounting for 40% of all non-Hodgkin lymphomas¹. DLBCL presents as an aggressive disease requiring immediate

Reprints and permissions information is available at www.nature.com/reprints.

Correspondence and requests for materials should be addressed to D.W.S. or C.S., dscott8@bccancer.bc.ca; CSteidl@bccancer.bc.ca.

Author contributions

D.E., S.H., A.B., R.D.G., S.P.S., D.W.S. and C.S. designed and performed the research, analyzed and interpreted data and wrote the paper; D.E. and A.J.M. performed library construction and DNA- and RNA-seq; S. Saberi analyzed and interpreted the genomic and transcriptome data and also contributed to some of the figures; C.H., F.C.C., L.C., D.L., A.W.Z., S. Salehi, G.D., C.R., R.D.M. and H.P.S. performed and supervised genomic and transcriptome data analysis; A.B., M.A.M. and R.D.M. provided bioinformatics assistance; S.H., T.A., N.W., N.D.S., R.S.M., L.L.M., M.Y.L. and K.T. performed in vitro and in vivo studies under the supervision of A.P.W. and M.B.B.; L.A. performed single-particle tracking studies under the supervision of M.G; M.W., N.N.V. and R.A.U. performed and helped SIRPα experiments; A.B., B.N.B., B.W.W., A.M. E.V. and A.T. designed, performed and validated experimental material; D.E., B.M., M.B. and S.B.-N. performed RNA and DNA extractions and FISH analysis; L.L.M. and R.S.M. performed flippase immunoprecipitations and activity assays; A.M., P.F., G.W.S. and R.D.G. performed pathological review of samples; A.M., P.F. and R.D.G. stained and scored IHC work; D.S.C., G.D., S.M. and G.V.C.F. analyzed clinical data and developed the prognostic model; D.W.H. and L.M.S. analyzed publicly available datasets; R.K., A.S.G., D.V., L.H.S., K.J.S. and J.M.C. assembled and interpreted clinical data; S.P.S., D.W.S., C.S. and R.D.G. supervised the study.

Extended data is available for this paper at <https://doi.org/10.1038/s41591-020-0757-z>.

Supplementary information is available for this paper at <https://doi.org/10.1038/s41591-020-0757-z>.

Online content

Any methods, additional references, Nature Research reporting summaries, source data, extended data, supplementary information, acknowledgements, peer review information; details of author contributions and competing interests; and statements of data and code availability are available at <https://doi.org/10.1038/s41591-020-0757-z>.

treatment, and current standard of care for patients treated with curative intent is multiagent chemotherapy in combination with rituximab, an anti-CD20 antibody (R-CHOP; rituximab, cyclophosphamide, doxorubicin, vincristine and prednisone)^{2,3}. Although considerable improvement in outcome has been achieved, ~40% of patients still experience treatment failure. We contend that further improvement of treatment outcome relies on elucidating the molecular determinants related to treatment response and survival in homogeneously treated cohorts that are representative of patients encountered in clinical practice.

Two major molecular subtypes of DLBCL are recognized, based on cell-of-origin (COO) classification: activated B-cell-like (ABC) and germinal center B-cell-like (GCB) subtypes. The COO subtypes have distinct underlying biology, clinical behavior and genetic features⁴⁻⁶. Several sequencing studies have identified candidate driver genes implicated in the differential pathogenesis of COO subtypes⁷⁻¹⁰. The most recent genomic landscape studies also suggested genetic subtypes of this entity¹¹⁻¹³, however, functional characterization and clinical correlates of genetic alterations are rarely available.

Here, we characterized the recurrent genetic alterations and transcriptomic signatures in diagnostic biopsies from a population-registry-based cohort of 347 patients with de novo DLBCL uniformly treated with R-CHOP. This analysis revealed biallelic *TMEM30A* mutations to be associated with favorable treatment outcome and loss of function. Using *TMEM30A*-mutant systems, we have discovered that *TMEM30A* loss is associated with increased B-cell receptor (BCR) signaling, and is correlated with increased BCR mobility. In addition, *TMEM30A* loss leads to increased drug accumulation and an increase in tumor-associated macrophage infiltration, potential molecular mechanisms underlying the favorable clinical outcomes associated with these mutations. We furthermore uncovered increased efficacy of CD47 blockade in *TMEM30A* mutant models, driving increased tumor-cell phagocytosis and improved survival. Our study identifies an important role of *TMEM30A* in lymphomagenesis, and elucidates new mutation-associated vulnerabilities that sensitize lymphoma cells to immunochemotherapy.

Results

Specific gene mutations are associated with outcome in DLBCL.

We analyzed diagnostic biopsies from the British Columbia Cancer registry-based population of 347 patients with de novo DLBCL treated with R-CHOP. The baseline characteristics and outcomes in the study cohort were similar to those of the entire population of patients with DLBCL ($n = 1,177$) treated with curative intent in BC during the study period (Supplementary Fig. 1). We catalogued the genetic alterations and transcriptomic signatures using deep-targeted amplicon sequencing ($n = 57$ genes), SNP6.0 arrays and RNA sequencing (RNA-seq) (Extended Data Fig. 1a,b, Supplementary Fig. 2 and Supplementary Tables 1–3).

First, we assessed the influence of individual recurrent genetic alterations on time to progression (TTP) and overall survival (OS) (Extended Data Fig. 2 and Supplementary Table 4). Mutations in *TMEM30A*, BTG anti-proliferation factor 1 (*BTG1*) and tumor protein p53 (*TP53*), as well as deletions in beta-2-microglobulin (*B2M*) and gain/amplifications in

nuclear factor of activated T cells 1 (*NFATC1*) were significantly associated with both TTP and OS in the entire cohort, and this was retained when controlling for the International Prognostic Index (IPI) and COO subtype (Fig. 1a and Supplementary Table 5). Furthermore, other genetic alterations were also significantly associated with both TTP and OS within only one COO subtype: microRNA 15a (*MIR15a*) and *MIR16-1* deletion in ABC-DLBCL, and gain and/or amplifications of cytochrome P450 family 2 subfamily E member 1 (*CYP2E1*) and *MYC*, and *TP53* mutation in GCB-DLBCL (Fig. 1b,c).

We also developed a prognostic model based on the selection and combination of genetic alterations using a stringent statistical methodology based on an adaptive lasso estimator for Cox's proportional-hazards model (Cox-lasso). Results demonstrate that the selected genetic alterations contained additional signals informative of TTP beyond COO and IPI. Genetic alterations that were repeatedly selected in most crossvalidation training sets included mutations of *TMEM30A*, *BCL6* and *TP53*, deletions of *INPP4B*, *PTEN* and *B2M*, gain/amplification of *NFATC1*, and *MYC* translocation (Fig. 1d).

Integrative analysis revealed *TMEM30A* as a putative tumor-suppressor gene.

We next performed an integrated mutation-gene expression analysis using xseq¹⁴, and identified loss-of-function mutations in *TMEM30A* that strongly influence expression in *cis* in the whole DLBCL cohort (Fig. 1e). Notably, more than 80% of tumors with *TMEM30A* mutations show hemizygous deletions and/or copy-neutral loss of heterozygosity, which was the most frequent co-occurrence among analyzed genes (Fig. 1f). In addition, most of the *TMEM30A* mutations (82%) are nonsense, splice-site and frameshift mutations, amounting to the highest proportion of truncating mutations among all evaluated genes (Fig. 1g). The inactivation pattern of *TMEM30A* mutations, in conjunction with the observed association with superior outcome, prompted us to further investigate the genetic, clinical and functional features in detail.

TMEM30A (*CDC50A*) encodes the beta-subunit of phospholipid flippase (P4-ATPase) and a component of flippase, which regulates translocation of phosphatidylserine (PS) from the outer to the inner leaflet of the plasma membrane, maintaining an asymmetric distribution of the phospholipid^{15,16}. In our cohort, *TMEM30A* mutations were scattered across all coding exons (Fig. 2a). Notably, 95% of *TMEM30A* mutations were located in the transmembrane and extracellular domains^{17,18} (Fig. 2b). We confirmed the somatic nature of the mutations in all five patients with available germline DNA. *TMEM30A* was mutated in 38/347 (11%) DLBCL patients, with similar frequency in ABC-DLBCL (12%) and GCB-DLBCL (11%). In total, *TMEM30A* genetic alterations were observed in 27% of DLBCL patients, including 31 patients with biallelic alterations (Fig. 2c,d).

A number of missense mutations in *TMEM30A* have been previously investigated, and were shown to result in a reduction in correct localization and flippase activity¹⁹. We similarly examined the ability of *TMEM30A* mutants, co-expressed with ATP8A2 in HEK293T cells, to heterodimerize and actively flip PS within the plasma membrane (Extended Fig. 3a). Using immunoprecipitation to test for complex formation, we observed that truncated *TMEM30A* mutants (R226X, R290X, R307X) did not precipitate with ATP8A2, suggesting a failure to form a complex. Missense *TMEM30A* mutants (C94R, D181Y)

were precipitated with ATP8A2, though there was an absence of higher-molecular-weight banding, suggesting a reduction in glycosylation—a modification necessary for normal complex formation and activity¹⁷. These missense mutants also demonstrated a reduction in flippase activity (Extended Fig. 3b).

***TMEM30A* mutations are correlated with concurrent loss of tumor-suppressor genes in chromosome 6q.**

GISTIC analysis identified chromosome 6q14.1, including the *TMEM30A* locus, as a significantly deleted site (Extended Fig. 1b and Supplementary Table 3). Of note, broad heterozygous deletions of chromosome 6q were found in the vast majority of affected patients, which includes other known tumor-suppressor genes in B-cell lymphoma, including *EPHA7*, *PRDM1* and *TNFAIP3* (Fig. 2e). Overall, 82% (31/38) of tumors with *TMEM30A* mutations and 95% (76/80) of heterozygous deletions had concomitant genetic alterations of *EPHA7*, *PRDM1* and *TNFAIP3* (Extended Fig. 3c). Furthermore, among recurrent mutations found in DLBCL, *TNFAIP3* and *PRDM1* mutations were significantly enriched in *TMEM30A* mutated tumors ($P=0.0002$ and $P=0.02$, respectively; Fisher's exact test) (Fig. 2f and Extended Fig. 3d).

We also calculated relative cancer-cell fraction (CCF), which compares *TMEM30A* copy number (CN) and mutation, revealing that CCF of 6q deletion was significantly higher than that of *TMEM30A* mutation ($P=0.003$: one-sample *t*-test). Specifically, among assessable events, 15 out of 22 (68%) 6q deletions had higher CCFs than the *TMEM30A* mutation, while CCFs with *TMEM30A* mutation were higher in only 6/22 (27%) (Fig. 2g). This analysis suggests that 6q deletions precede *TMEM30A* mutations in the majority of DLBCL patients.

***TMEM30A* mutation uniquely occurs in DLBCL and confers favorable outcome.**

Next, we searched publicly available datasets and found that *TMEM30A* mutations were recurrently found in aggressive B-cell lymphomas (DLBCL, transformed follicular lymphoma (tFL) and primary CNS lymphoma) with similar mutation patterns as in our dataset. In contrast, mutations were rarely observed in Burkitt lymphoma and FL, and absent in other hematologic malignancies (Fig. 3a). In non-hematological malignancies, *TMEM30A* was exceedingly rarely mutated (0.3% of nearly 10,000 patients) (Supplementary Table 6).

Our previous analysis of 118 patients with paired diagnostic and transformed FL specimens showed that *TMEM30A* mutations were found at the time point of transformation to DLBCL (T2), but not at primary diagnosis (T1) in 6 patients²⁰ (Fig. 3b and Extended Data Fig. 4a,b). Moreover, in 1 case of FL recurrence after transformation, *TMEM30A* mutation was found with a low allele frequency (1.6%) at the time of recurrence (T3; histology of FL). These data demonstrate that *TMEM30A* mutations were acquired during transformation and not found in FL.

Tumors harboring *TMEM30A* mutations were significantly associated with a favorable outcome in our cohort (Fig. 3c, and Extended Fig. 4c,d). Notably, the prognostic effect of *TMEM30A* mutations was particularly evident when examining the outcomes in patients

with high IPI scores (Fig. 3d and Extended Fig. 4e). In addition, patients with *TMEM30A* biallelic alteration showed significantly longer TTP compared to those with the wild type ($P = 0.035$; log-rank test), whereas patients with monoallelic alterations had similar outcomes to those with wildtype *TMEM30A* (Fig. 3e). There were no significant differences in clinical and phenotypic characteristics according to *TMEM30A* biallelic mutations (Supplementary Table 7). Interestingly, *TMEM30A* mutations were detected as a significant component of mutation-defined, genetic subtypes with favorable outcomes in two recent studies (BN2 and C1 groups)^{12,13}.

Basal phosphatidylserine exposure is unchanged in DLBCL *TMEM30A*-knockout cells.

These results suggest that *TMEM30A* is a previously unknown tumor suppressor in DLBCL, whose loss is associated with favorable outcome in patients. To characterize functional mechanisms at play, we generated *TMEM30A* knockout cell lines (*TMEM30A*^{-/-}) using CRISPR-Cas9 genome editing in two GCB-DLBCL cell lines (DOHH-2, Karpas422), and one ABC-DLBCL cell line (NU-DUL-1) (Supplementary Table 8 and Extended Data Fig. 5a). As an established control, we also generated *TMEM30A*^{-/-} in Jurkat, a T-cell lymphoblastic line²¹. In the absence of a reliable *TMEM30A* antibody, we verified lower messenger RNA and protein expression by qPCR, RNA-seq and global proteomics analysis (Extended Data Fig. 5b–d and Supplementary Table 9). Expression levels of P4-ATPases, *TMEM30B* and *TMEM30C* in wildtype and *TMEM30A*^{-/-} cell lines using RNA-seq, were found to be unchanged (Extended Fig. 5d).

We examined PS extracellular exposure in cycling, untreated *TMEM30A*^{-/-} cells with annexin V binding. As previously established, *TMEM30A* loss of function in Jurkat cells showed a significant increase in PS exposure²¹ (Fig. 4a). Comparatively, PS exposure was only minimally increased or absent in DLBCL *TMEM30A*^{-/-} cells.

TMEM30A-knockout cells show increased BCR mobility and B-cell receptor signaling.

It is unknown whether *TMEM30A* loss has a role in primary selection and lymphomagenesis in DLBCL. We therefore investigated the role that *TMEM30A* loss-of-function might play in BCR-dependent signaling driving lymphomagenesis. Using single-particle tracking, we found that the lateral mobility of cell surface IgG BCRs, which regulates the strength of BCR signaling, was found to be 2- to 5-fold higher in *TMEM30A*^{-/-} cells, though surface expression of IgG BCRs was equivalent^{22–26} (Fig. 4b and Extended Data Fig. 6a). IgG BCRs in *TMEM30A*^{-/-} cells traversed larger areas on the cell membrane, as measured by the increased confinement diameter of these tracks (Fig. 4c and Extended Data Fig. 6b). Since BCRs transiently move faster or slower as they explore the local membrane environment, we used a two-state hidden Markov model (HMM) that subdivides receptor trajectories into fast and slow diffusive modes, each characterized by a single diffusion coefficient²⁷. In *TMEM30A*^{-/-} cells, there was an increased fraction of IgG BCRs in the inferred fast state (Fig. 4d and Extended Data Fig. 6c), and a higher rate of transitioning/switching from a slow-to-fast state ($K_{\text{slow} \rightarrow \text{fast}}$) than in wild-type cells (Fig. 4e and Extended Data Fig. 6d). We repeated this analysis with CD19, an important coregulator in B-cell signaling. However, CD19 mobility was not altered in *TMEM30A*^{-/-} cells, suggesting the increase in diffusion was BCR-specific (Extended Data Fig. 6e, f).

We next stimulated wild-type and *TMEM30A*^{-/-} DLBCL cells with bivalent F(ab)₂ antibody fragments as a surrogate antigen, inducing T-cell-independent B-cell signaling. We observed a dramatic increase in PS exposure in *TMEM30A*^{-/-} cells, but not wild-type cells, following stimulation (Fig. 4f,i). A similar response was observed following ionomycin treatment (Fig. 4g,i). This increase was not found to be correlated with a decrease in viability or an increase in apoptotic signaling (Extended Data Fig. 6g). Intracellular calcium was increased, with no significant difference between wild-type and knockout cell lines (Extended Fig. 6h).

To evaluate the role of BCR stimulation in PS exposure, we blocked the signaling cascade by preincubating DOHH-2 cells with ibrutinib, a BTK inhibitor. DOHH-2 and GCB-DLBCL in general are largely resistant to ibrutinib²⁸, and we similarly observed non-toxic effects under experimental and CRISPR-Cas9 screen conditions (Extended Data Fig. 7a,b)²⁸. We recorded a reduction in F(ab)₂-fragment-induced calcium release following ibrutinib inhibition, indicating a blockade of downstream signaling events (Extended Data Fig. 7c). Moreover, we observed a significant reduction in F(ab)₂-fragment-induced PS exposure in *TMEM30A*^{-/-} cells with ibrutinib treatment, indicating a direct role of BCR signaling in PS exposure (Extended Data Fig. 7d).

TMEM30A-loss-induced differences in downstream BCR signaling events were investigated, and found to be varied in different cell lines. In Karpas422 *TMEM30A*^{-/-} cells, incubation with F(ab)₂ fragments caused a significantly greater increase in the expression of surface markers, such as CD69 (Fig. 4f,ii and Extended Data Fig. 7e). Both AKT and ERK1/2 showed increased levels of phosphorylation in stimulated NU-DUL-1, and to a more limited extent in Karpas422 *TMEM30A*^{-/-} cells (Fig. 4f,iii and Extended Data Fig. 7f). Taken together, TMEM30A loss-of-function enhances cell surface BCR dynamics facilitating more rapid B-cell responses after BCR crosslinking and/or antigen binding.

Given the connection between TMEM30A loss, increased BCR dynamics, calcium release and PS exposure, we studied the role for calcium-induced scramblases, such as TMEM16F (encoded by *ANO6*), in influencing the PS equilibrium²⁹. Scramblases play a predominant role in flipping PS to the extracellular side of the plasma membrane, opposing flippase activity³⁰⁻³⁵. Expression levels of *ANO6* and other scramblases were observed to be unchanged between *TMEM30A*^{-/-} and wild-type cells (Extended Data Fig. 5d). To examine the role of TMEM16F, we generated *ANO6* frameshift mutants using CRISPR-Cas9 gene editing (*TMEM16F*^{F/+}, Supplementary Table 8 and Extended Data Fig. 5e). We did not observe any alteration in basal levels of PS exposure in *TMEM30A*^{-/-} cells. However, we found a significant decrease in ionomycin-induced PS exposure in *TMEM30A*^{-/-} *TMEM16F*^{F/+} cells, and with a similar trend following F(ab)₂ induction (Fig. 4g,i,ii). These data suggest that TMEM16F, induced by increases in calcium following BCR stimulation, is the predominant driver of PS exposure following BCR activation.

TMEM30A-mutant cells show increased sensitivity to chemotherapy drugs.

Given the favorable treatment outcome of patients with DLBCL with TMEM30A loss, we examined PS exposure in *TMEM30A*^{-/-} DLBCL cell lines after treatment with doxorubicin and vincristine. We observed a two-fold increase in PS externalization in *TMEM30A*^{-/-} cells relative to controls following treatment (Fig. 5a,i). We also included a *TMEM30A*^{-/-}

‘rescued’ line, by reintroducing a native TMEM30A expressing vector (‘rhTMEM30A’) into a TMEM30A^{-/-} cell line (Extended Fig. 5c). A TMEM30A dependent reversal of drug-induced PS exposure was seen in TMEM30A^{-/-}+rhTMEM30A, compared with the empty vector control (+Empty) (Fig. 5a, ii).

PS extracellular exposure is an endpoint response to apoptotic signaling following the activation of caspase-3, which deactivates TMEM30A and activates scramblases^{34,35}. Apoptotic activation following doxorubicin and vincristine treatment was compared in TMEM30A^{-/-} and control cells by detecting caspase-3 activation. TMEM30A^{-/-} cells demonstrated a higher quantity of caspase-3 activation relative to controls and rescued cells following drug treatment, confirming a higher level of apoptotic response in mutant cells (Fig. 5b,i). When treated with vincristine, a microtubule polymerization inhibitor, TMEM30A^{-/-} and empty rescue vector controls showed a higher population of arrested cells at the G2/M phase relative to wild-type controls and rescued cells (Fig. 5b,ii). Internalization of doxorubicin, which is naturally fluorescent and measurable by flow cytometry, allowed tracking of transport into the cell. After 2–4 h incubation, doxorubicin uptake was significantly higher in TMEM30A^{-/-} than in control cells (Fig. 5c).

We repeated this analysis with primary tumor cell suspensions from patients with DLBCL with TMEM30A biallelic alterations, compared with TMEM30A normal cells. As in the mutant cell lines, the primary tumor cells with TMEM30A mutations demonstrated higher PS exposure after doxorubicin treatment and doxorubicin uptake was significantly higher in TMEM30A-mutated tumors relative to their normal counterparts (Fig. 5d,e). Taken together, these results show that the TMEM30A loss of function results in stress-induced enhanced PS exposure, doxorubicin uptake and apoptosis in genome-edited cell lines and primary tumor B cells.

XKR8 is a primary scramblase catalyzing PS exposure during apoptosis in lymphocytes^{35,36}. To evaluate the role of PS exposure in doxorubicin uptake, we generated XKR8 mutants (XKR8^{-/-}) in the cell line NU-DUL-1, using CRISPR–Cas9 gene editing (Supplementary Table 8 and Extended Data Fig. 5e). Basal levels of PS exposure in TMEM30A^{-/-}XKR8^{-/-} were found to be unchanged relative to TMEM30A^{-/-} (Fig. 5f,i). However, following doxorubicin treatment, PS exposure was found to be significantly blocked in both the XKR8^{-/-} cell line with wild-type TMEM30A and the TMEM30A^{-/-}XKR8^{-/-} cell line, indicating a primary role for XKR8 in PS exposure following chemotherapeutic treatment (Fig. 5f,i). Doxorubicin uptake was slightly, though significantly, reduced in XKR8^{-/-} cell lines (Fig. 5f,ii).

Xenotransplantation of human TMEM30A^{-/-} cells in mouse models shows tumor regression and improved survival with vincristine.

DOHH-2 TMEM30A^{-/-} cells, subcutaneously injected into immune-deficient NOD-scid IL2Rgnull (NSG) mice, exhibited reduced tumor growth and increased survival relative to wild-type controls, despite equivalent proliferation rates in vitro (Extended Data Fig. 8a). Xenotransplanted mice treated with vincristine demonstrated a longer survival rate (Fig. 6a) and reduced tumor growth rates in both wild-type and mutant groups (Extended Data Fig. 8b). Mice with wild-type DOHH-2 succumbed to their tumors after 24–27 d, with vincristine

significantly extending survival. Interestingly, *TMEM30A*^{-/-} xenografts demonstrated a dramatic response to vincristine. Following treatment, 4 out of 5 mice with *TMEM30A*^{-/-} DOHH-2 responded favorably to vincristine, showing substantial tumor regression, and in 3 cases complete disappearance of the tumor by the end of this study (Day 76) (Extended Fig. 8b). These xenotransplantation models recapitulated the improved prognosis seen in patients with biallelic *TMEM30A* mutations with demonstration of increased sensitivity to chemotherapy and improved outcomes compared with wild-type controls.

Increased macrophage infiltration and phagocytosis associated with *TMEM30A* loss of function.

The role of externalized PS in macrophage recognition and engulfment prompted us to examine the effects of *TMEM30A* loss of function on phagocytosis. To further examine the association of macrophages with *TMEM30A*^{-/-} cells in an immune competent model system, we generated a syngeneic mouse model utilizing the murine B-cell lymphoma cell line A20, a highly aggressive tumor cell line from a Balb/cAN mouse resembling a mature B-cell neoplasm with characteristics of DLBCL (Supplementary Table 8). The growth rate of mutant (*Tmem30A*^{-/-}) and control cell lines were equivalent, and *Tmem30A*^{-/-} cells showed slightly higher PS exposure than did wild-type cells (Extended Data Fig. 9a, b). Balb/c mice injected with *Tmem30a*^{-/-} cells survived longer than those injected with wild-type cells, though proliferation by Ki-67 staining was equivalent (Fig. 6b and Extended Data Fig. 9c). Tumor infiltrates were present in multiple organs (liver, spleen, lung) in the control group, with reduced or no infiltrate in the *Tmem30A*^{-/-} groups (Extended Data Fig. 9d–f). Interestingly, we observed a significantly increased level of macrophage infiltrates in *Tmem30A*^{-/-} tumors at an earlier stage in tumor development compared with controls, following both intravenous and subcutaneous implantation of A20 cells (Fig. 6b,c and Extended Fig. 9g). We also found that CD163 staining was absent in control and *Tmem30A*^{-/-} tumors, suggesting that these tumor-associated macrophages were predominantly M1 polarized (Fig. 6b). RNA-seq of tumor tissue also revealed significantly reduced expression of interleukin 4 induced 1 (*Il4i1*) (false-discovery rate (FDR) = 2.43×10^{-6}), which is a representative M2 macrophage marker, in *Tmem30A*^{-/-} tumors compared with control tumors (Extended Data Fig. 9h i). Our data suggest that *TMEM30A* loss of function is associated with a primed microenvironment for phagocytosis.

Enhanced efficacy of CD47 blockade limiting tumor growth in *TMEM30A*-knockout models.

We then elected to investigate the efficacy of a phagocytic checkpoint inhibitor in vitro and in vivo. Specifically, we tested SIRP α Fc (TTI-621), a new CD47 blockade drug currently undergoing assessment in clinical trials³⁷. CD47 is characterized as a ‘don’t eat me’ signal, which blocks phagocytosis through a direct interaction with the SIRP α receptor expressed on macrophages³⁸. TTI-621 acts both as a competitive CD47 block and as an opsonizing agent via a fused IgG1 Fc domain³⁷. First, we tested the ability of TTI-621 to increase the in vitro phagocytosis index of DLBCL cell lines, compared with TTI-402, a negative control (IgG Fc), using macrophage co-culture assays (Fig. 6d). From this evaluation, TTI-621 induced increased phagocytosis of DOHH-2, with significantly enhanced engulfment of *TMEM30A*^{-/-} cells.

Finally, we evaluated TTI-621 or TTI-402 in our DOHH-2 xenograft model. As before, DOHH-2 *TMEM30A*^{-/-} xenografts showed increased macrophage infiltrates relative to the control treatment group, with higher levels observed following TTI-621 treatment, including a measurable increase in observed engulfed cells (Fig. 6e and Extended Data Fig. 8c). Mice treated with TTI-621 showed prolonged survival compared with mice treated with TTI-402 (Fig. 6f), with a significant reduction in tumor growth (Extended Data Fig. 8d). Significantly, TTI-621 treatment enhanced the survival of *TMEM30A*^{-/-} xenografts compared with wild-type xenografts, with a concurrent stall in tumor growth that was significantly more prolonged in *TMEM30A*^{-/-} than in wild-type cells (Fig. 6f and Extended Data Fig. 8d).

Discussion

Our integrative genomic and transcriptomic analyses of tumors from 347 patients with DLBCL highlighted new biallelic loss-of-function mutations of *TMEM30A*, a gene that has not previously been implicated in cancer in detail. *TMEM30A* mutations are significantly associated with favorable outcome, and are uniquely found in DLBCL. Through functional analysis in mutant cell lines, primary lymphoma cells and mouse model systems, we demonstrated biological mechanisms that underlie the primary selection of B-cell lymphoma development, and the favorable outcome of patients with *TMEM30A*-mutated DLBCL. Of therapeutic importance, *TMEM30A* mutation was associated with macrophage engulfment using CD47 blockade. These findings suggest predictive value of *TMEM30A* mutation status and related macrophage biology in the context of new checkpoint inhibitor treatments.

The present study was conducted in a large, uniformly R-CHOP-treated DLBCL cohort derived from a population-based registry, allowing us to perform precise molecular mapping of recurrent genetic alterations and to investigate their clinical significance. Our integrative genomics approach and stringent statistical modeling identified biallelic *TMEM30A* loss-of-function mutations as functionally important, and intriguingly associated with superior outcome. Furthermore, this favorable prognosis of *TMEM30A* loss was also observed across multiple datasets^{12,13}. Of importance, GISTIC analyses in our and other studies¹² similarly detected the minimum commonly deleted region of 6q14.1 harboring only a few tumor suppressor genes, including *TMEM30A*, in DLBCL highlighting this locus as biologically relevant in the context of broader scale 6q deletions.

Our finding of *TMEM30A* mutational specificity to DLBCL may be explained by increased BCR clustering and signaling which were shown in our DLBCL *TMEM30A*-mutant model systems, which represents a mechanism of selective advantage for B-cell lymphoma development. Emerging concepts of tuning B-cells via increased lateral mobility of BCRs and their interaction with positive regulators/co-receptors have been proposed^{22,25}. Here we show that *TMEM30A* loss-of-function correlates with increased BCR spatial dynamics, and subsequently higher B-cell signaling/responses post BCR cross-linking. While we have yet to elucidate a mechanism connecting *TMEM30A*, PS exposure, membrane physiology and BCR signaling, various observations demonstrating PS enrichment in lipid rafts, which house the BCR signalosome, and potential indirect connections between PS and the actin cytoskeleton suggest an emergent role that has yet to be discovered³⁹⁻⁴².

Another prominent finding of this study is increased drug sensitivity in the TMEM30A mutant models and the primary lymphoma cells. Regulating membrane transportation is an important biological role of the P4-ATPase and TMEM30A complex^{15,43} and in previous studies, TMEM30A was shown to control the uptake of anti-cancer drugs, suggesting its key role in the transport of chemotherapeutic agents across the plasma membrane^{44,45}. One study in particular connected an increase in PS exposure with an increased uptake of BODIPY-taxol, and proposed a role of membrane morphology in this change in uptake⁴¹. We similarly demonstrated that TMEM30A inactivation enhanced the uptake of doxorubicin leading to increased apoptosis.

Surface PS has been well characterized as an ‘eat me’ signal, recognized by macrophages and stimulating engulfment. Several therapeutic agents, including rituximab, antibodies targeting PDL1 or CD47, have utilized this mechanism to target tumor cells for macrophage clearance. Indeed, a recent clinical trial has demonstrated dramatic anti-lymphoma effects with CD47 blockade in patients with DLBCL⁴⁶. We have observed *TMEM30A*-mutation-associated increases in macrophage engulfment in vitro, macrophage infiltration and reduced tumor growth in vivo. Interestingly, our models demonstrated significantly prolonged survival in combination with cytotoxic treatment (vincristine) or CD47 blockade (TTI-621). It stands to reason that patients with DLBCL with TMEM30A loss may be excellent candidates for CD47 blockade trials.

In conclusion, our study uncovered clinically relevant mutations in a cohort representative of patients with DLBCL encountered in clinical practice. This is the first study to demonstrate a clinical and biological role of TMEM30A in human cancer, providing new biological insights into membrane physiology in B-cell lymphoma development and mutation-associated cellular vulnerabilities.

Methods

Patient cohort description.

Initially, the BCCA Lymphoid Cancer database was searched to identify all patients with DLBCL diagnosed between 1985 and 2011. From 4,063 patients with DLBCL, 347 with de novo DLBCL were included in the final cohort for analysis if they met the following criteria: patients had to be 16 years of age or older, treated uniformly with R-CHOP with curative intent at BC Cancer, had complete clinical, laboratory and outcome data available, and had a fresh frozen diagnostic biopsy. The diagnosis was made according to the 2008 World Health Organization classification, as determined by standardized review by expert hematopathologists (A.M., P.F., G.W.S. and R.D.G.)⁴⁷. Patients were excluded if they had any of the following: primary mediastinal large B-cell lymphoma; primary or secondary central nervous system involvement at diagnosis; a previous diagnosis of an indolent lymphoproliferative disorder; positive HIV serology; a secondary malignancy or major medical comorbidity that precluded treatment with curative intent (Supplementary Fig. 1a). The baseline characteristics and outcomes in the study cohort were similar to those of the entire population of patients with DLBCL ($n = 1,177$) treated with curative intent in BC during that time, with the exception that there was a significantly lower proportion of patients with two or more extranodal sites in the study cohort as described previously⁴⁸. This

study was reviewed and approved by the University of British Columbia, British Columbia Cancer Agency Research Ethics Board, in accordance with the Declaration of Helsinki.

Targeted sequencing.

Mutational data were generated based on deep targeted sequencing using Truseq Custom Amplicon assay (mean coverage, 767; range, 128–2,039; s.d., 180). For the validation of detected variants, we also performed deep-targeted sequencing with Fluidigm Access Array system.

We sequenced the protein-coding regions of 59 genes in 347 tumors and matched 67 normal samples using deep targeted sequencing. Using our mutation data previously generated and published⁷, along with the other 2 published DLBCL mutation landscape reports^{8,9}, we selected 59 genes for the deep targeted re-sequencing, which included recurrently mutated genes at: (1) >5% in at least two studies; (2) >10% in one study; and (3) biological interest. The genes are: *ACTB*, *ARHGEF1*, *B2M*, *BCL2*, *BCL6*, *BCL7A*, *BCR*, *BRAF*, *BTG1*, *BTG2*, *CARD11*, *CCND3*, *CD274*, *CD36*, *CD58*, *CD70*, *CD79B*, *CD83*, *CIITA*, *CPS1*, *CREBBP*, *EP300*, *EZH2*, *FOXO1*, *GNA13*, *HIST1H1C*, *HIST1H1E*, *HIST1H3B*, *HLA-C*, *IFR8*, *KLHL6*, *KMT2D*, *KRAS*, *MEF2B*, *MKI67*, *MYC*, *MYD88*, *MYOM2*, *NLR5*, *NOTCH1*, *P2RY8*, *PCLO*, *PIMI1*, *PRDM1*, *RFXAP*, *RHOA*, *S1PR2*, *SETD2*, *SGK1*, *STAT3*, *TMEM30A*, *TMSL3*, *TNFAIP3*, *TNFRSF14*, *TNFSF9*, *TP53*, *UNC5C*, *UNC5D*, *ZFP36L1*. The 5% threshold for incidence was based on a calculation of power to detect survival differences in a cohort size of 347 patients at varying hazard ratios and mutational incidences (Supplementary Table 1). This table indicates that there would be limited power to detect survival differences between groups where the mutational incidence is below 5%.

We used two orthogonal deep sequencing strategies (Fluidigm Array and TSCA) for the validation of single-nucleotide variants (SNV) and insertions/deletions (indels). 1,914 SNVs and indels identified using TSCA were selected to design a Fluidigm assay to evaluate the sensitivity of the TSCA assay. Among 1,914 SNVs sequenced, 1,884 SNVs were qualified to be evaluated, and 1,821 SNVs were confirmed to be present in the data from the Fluidigm assay, suggesting a validation rate of 97% (1,821/1,884).

The final mutation list included 3,164 nonsynonymous variants, including 2,520 missense, 243 nonsense, 139 splice site mutations and 262 indels (Supplementary Table 2). When the above filtering process was applied to matched-tumor normal samples ($n = 67$), 395/419 true-positive somatic variants were detected with a sensitivity of 95%. Details are available in the Supplementary Methods.

SNP6.0-based copy-number analysis.

DNA samples from 338 DLBCL tumors were analyzed with Affymetrix Human SNP6.0 Array (Affymetrix, USA). 500 ng genomic DNA from fresh frozen specimens was labeled, fragmented and hybridized to microarrays using the manufacturer's recommended protocol. Affymetrix Human SNP 6.0 Array contains >946,000 non-polymorphic CNV probes. The staining and washing was carried out on a Fluidics Station 450 (Affymetrix) and scanning with a GeneChip scanner 3000 7G system (Affymetrix). CEL files were generated by

Affymetrix Command Console version 3.0. A detailed process of analyses is described in the Supplementary Methods.

Gene-expression analysis.

We obtained RNA-seq data for 322 DLBCL samples to quantify the gene-expression levels. Between 849 ng and 2 µg of total RNA were arrayed in a 96-well plate. Polyadenylated (polyA+) mRNA was purified using the 96-well MultiMACS mRNA isolation kit on the MultiMACS 96 separator (Miltenyi Biotec) then ethanol-precipitated, and used to synthesize complementary DNA using the Maxima H Minus First Strand cDNA Synthesis kit (Thermo-Fisher) and random hexamer primers at a concentration of 5 µM along with a final concentration of 1 µg µl⁻¹ Actinomycin D, followed by Ampure XP SPRI bead purification on a Biomek FX robot (Beckman-Coulter). The second-strand cDNA was synthesized following the Superscript cDNA Synthesis protocol by replacing the dTTP with dUTP in dNTP mix, allowing the second strand to be digested using uracil-*N*-glycosylase (UNG; Life Technologies) in the post-adaptor ligation reaction and thus achieving strand specificity. cDNA was fragmented by sonication using a Covaris LE220 (Covaris). Plate-based libraries were prepared using the Biomek FX robot (Beckman-Coulter) according to the British Columbia Cancer Agency, Genome Science Centre paired-end protocol, previously described. The purified libraries with a desired size range were purified and diluted to 8 nM, and then pooled at five per lane and sequenced as paired-end 75-bp on the HiSeq 2500 platform. This yielded, on average, 71 million reads per patient (range, 6.5–163.7 million reads). Details are available in the Supplementary Methods.

Survival analysis.

We evaluated the prognostic effect of mutations with a frequency of >5%, and representative CNAs within GISTIC regions. For survival analysis and comparison of frequencies between COO subtypes, we used gene-centric CNAs defined by OncoSNP. The patients with gain and/or HLAMP would be combined into one group as amplification, and HETD and HOMD were combined into one group as deletion since the frequencies of HLAMP and HOMD were very low. The Kaplan–Meier method was used to estimate the TTP (progression/relapse or death from lymphoma or acute treatment toxicity), progression-free survival (progression/relapse or death from any cause), disease-specific survival (death from lymphoma or acute treatment toxicity) and OS (death from any cause), with log-rank test performed to compare survival curves. In this study, we mainly used TTP, as this seems to be more sensitive to reflect the influence of genetic features on tumor progression by removing the death events not caused by lymphoma. Univariate and multivariate Cox proportional-hazards regression models were used to evaluate proposed prognostic factors.

Molecular-based prediction model.

We developed a genetic multivariate score based on 57 gene mutations, *MYC*, *BCL2* and *BCL6* translocations and CNAs. For this analysis, CNAs were selected based on representative genes within GISTIC in terms of known functional importance, as well as high driver probabilities of *cis* and/or *trans* effect (driver probability > 0.8) predicted by xseq analysis. In total, 3042 genes proceeded with this analysis. Since many of the molecular features were highly correlated, we grouped the information of correlated genes

into ‘metagenes’ using hierarchical clustering with Gower’s similarity and average linkage. The associated dendrogram was pruned at a height such that the number of tree nodes was approximately 100. This process downsized the variables of all genetic alterations into 98 metagenes.

We developed a computational pipeline to identify a genetic signature that can predict survival after adjusting for the presence of COO subtype and IPI index. Our pipeline started with a univariate selection of relevant genes, that is, for every metagene. We fitted a Cox proportional-hazards additive model that included a genetic feature and controls for the effect of COO and IPI. We selected all the metagenes whose Wald *P* values were less than 0.05. In the second step of our pipeline, we used the whole subset of significant metagenes, together with COO and IPI, to identify a genetic panel that explained TTP using a Cox–lasso. To avoid overshrinkage, we used a penalization level that was half-way between the lambda that minimizes the cross-validated error (that is., lambda.min in ‘glmnet’ R package) and the lambda such that the error was within one standard error of the minimum (that is, lambda.1se). Since this value was based on a tenfold crossvalidation, we used the average value from ten crossvalidation runs. The coefficients of the genetic variables, estimated by the resulting Cox–lasso, were used to build a continuous linear genetic score, which was further discretized at the median value in the corresponding training set. We assessed the statistical significance of this discrete genetic predictor by using a likelihood ratio test (LRT) to compare a Cox proportional-hazards model with only COO and IPI versus a model with COO, IPI and the genetic predictor. To control for over-fitting, we used leave-one-out cross-validation to select genes and estimate their coefficients in the training set, and used the resulting coefficients to build the predictive score for the test sample left out.

***TMEM30A* mutation in publicly available dataset.**

The frequency of *TMEM30A* mutations in different lymphoid malignancies was calculated utilizing data curated from 150 published studies that have reported somatic mutations in these cancers. The reported mutations ($n > 400,000$) from over 10,000 individuals were harmonized using TransVar (<https://bioinformatics.mdanderson.org/transvar/>) and subsequently annotated using VarScan (<http://varscan.sourceforge.net/>). All mutations present at a prevalence of >0.0001 among human donors were identified among exomes from nonmalignant blood samples (<http://exac.broadinstitute.org/>) and removed from the harmonized dataset as were variants present in dbSNP (<https://www.ncbi.nlm.nih.gov/snp/>). Known cancer hotspot mutations (<https://www.cancerhotspots.org/#/home>) were retained. These curated data will be made available through an open access ‘LymphoDB’ web site (D.W.H. and L.M.S., unpublished observations).

Cell lines and mice.

Human DLBCL cell lines DOHH-2 and Karpas422 were purchased from DSMZ and ATCC, respectively, and maintained in RPMI-1640 (Life Technologies) containing 10% or 20% FBS (Life Technologies), respectively. The mouse cell line A20 was provided by A. Beilhack (University of Würzburg, Germany), and maintained in RPMI-1640 containing 10% FBS. NU-DUL-1 was provided by M. Dyer (University of Leicester, UK), and maintained in RPMI-1640 containing 10% FBS. The Jurkat cell line was provided by A. Weng (BC

Cancer, Vancouver, Canada), and maintained in RPMI-1640 containing 10% FBS, 1% sodium pyruvate and 1% nonessential amino acids (all from Life Technologies). HEK293-T cells were purchased from Open Biosystems, and cultured in DMEM plus 10% FBS. For all studies, FBS was heat inactivated, by heating serum at 56 °C for 30 min before addition to medium. NSG mice were purchased from an in-house source (Animal Resource Centre, BC Cancer, Vancouver, BC). Balb/c mice were purchased from Envigo. All mouse studies were approved by the Institutional Animal Care Committee (IACC) at the University of British Columbia, in accordance with the Canadian Council on Animal Care Guidelines. This study was approved by the Research Ethics Board of the University of British Columbia and the BCCA, conducted in accordance with the Declaration of Helsinki. Details are available in the Supplementary Methods.

Xenotransplantation, syngeneic mouse modeling and tumor monitoring.

DOHH-2 cell lines were verified to be mycoplasma negative using the Venor GenM Mycoplasma Detection kit (Sigma Aldrich). Four million cells were resuspended 1:1 with 100 µl matrigel HC (Corning) and RPMI-1640 plus 10% FBS, and held on ice until injection. Cells were implanted subcutaneously into the back of each female NSG mouse using a 27-gauge needle. Tumor growth was monitored every second day by measuring tumor dimensions with calipers beginning with the observance of palpable tumors (100 mm³). When tumors are palpable, mice were randomly selected from each group (control, *TMEM30A*^{-/-}) for vincristine treatment at a concentration of 0.1 mg kg⁻¹, TTI-621 at a concentration of 10 mg kg⁻¹, or TTI-402 at a concentration of 6.67 mg kg⁻¹. Treatment (vincristine or saline control) were administered by injection (200 µl per 20-g mouse) in the tail vein every 4 d for a total of 3 injections (Q4D×3). Weekly thawed TTI-621 and TTI-402 was administered intraperitoneally (200 µl per 20 g mouse) on Monday/Wednesday/Friday for 4 weeks, for a total of 12 injections.

A20 cells were verified to be mycoplasma negative, as above. One million cells were resuspended in HBSS (Invitrogen) plus 10% FBS, and held at room temperature until injection. Cells were injected subcutaneously, in the shoulder or intravenously in the tail vein using a 28-g needle. Tumor growth was monitored as described above.

Mice were observed daily and euthanized when they appeared in poor health or when tumors grew to a maximum of 800 mm³. Tumor volumes were calculated according to the equation: length × width × height / 2, with length (mm) as the longest axis of the tumor. Mice were euthanized by isoflurane overdose followed by CO₂ asphyxiation. All mouse immunohistochemistry was performed as described above using antibodies of B220 (RA3-6B2; Thermo Fisher Scientific), Ki-67 (SP6; Abcam), F4/80 (D2S9R; Cell Signaling Technology) and CD163 (EPR19518; Abcam).

In vitro macrophage engulfment assay.

Human monocytes were isolated from fresh, commercial human normal peripheral blood B cells (ZenBio) as follows. Cells were washed twice in PBS and resuspended in PBS/1% FBS at a final density of 1 × 10⁷ cells per ml. Twenty microliters of CD14 MicroBeads (Miltenyi Biotec) per 1 × 10⁷ cells were added and incubated at 4 °C for 15 min. CD14⁺ cells were

then collected by magnetic separation with a MACS Separator using two sequential LS columns, following manufacturer's directions (Miltenyi Biotec). Cells were counted, and the CD14⁺ enrichment of the final cell culture was assessed by flow cytometry, by staining with anti-human CD14-APC (eBioscience). Two million cells were plated in a 6-well plate, and cultured for 1 week in X-VIVO15 medium (Lonza) plus 20 ng ml⁻¹ recombinant human M-CSF (PeproTech). The cells were thusly maintained for up to 4 weeks, and medium was changed every 3–4 d.

One day before the phagocytosis assay, monocyte-derived macrophages (MDMs) were primed by adding 100 ng ml⁻¹ human IFN- γ (PeproTech). The following day, primed macrophages were detached by rinsing wells with 2 mM EDTA/PBS, followed with incubation in enzyme-free cell dissociation buffer (Gibco). Detached cells were washed twice in X-VIVO15/rhM-CSF medium, and 50,000 cells were seeded in a 96-well round-bottom plate.

Viable DOHH-2 cells, the target cells for macrophage engulfment, were washed twice in PBS, and labeled with pH-tolerant Violet Proliferation Dye VPD450 (BD Biosciences), by incubation with 1 μ M dye with 1×10^6 cells (37 °C, 15 min). The labeling reaction was quenched with heat inactivated FBS, and the cells were washed four times in PBS and resuspended in X-VIVO15/rhM-CSF media. Labeled cells were then treated with 1 μ M TTI-621 or TTI-402 for 30 min at 37 °C. Following treatment, cells were combined with aliquoted macrophages, allowing phagocytosis to occur for 2 h at 37 °C. The extent of phagocytosis following incubation was measured by flow cytometry. The assay plate was washed twice with cold FACS buffer (2 mM EDTA, 2% heat inactivated FBS, 0.1% sodium azide, in PBS). Human FcR binding inhibitor (eBioscience) was added to each well and incubated for 10 min at room temperature. Cells were then labeled for 30 min on ice for macrophage detection with the following panel: anti-human CD11b-PE (eBioscience), anti-human CD14-APC, and Live/Dead Fixable Near-IR Dead2 Cell Stain (Life Technologies). The assay plate was then washed four times in FACS buffer, and cells were resuspended in stabilizing fixative solution (BD Biosciences). CD11b⁺CD14⁺ macrophages were gated and tested for the presence of engulfed DOHH-2 cells (high VPD450) as an indication of phagocytosis. All samples were acquired using an LSRFortessa and analyzed using FlowJo Version V10.2 software.

Statistical analysis.

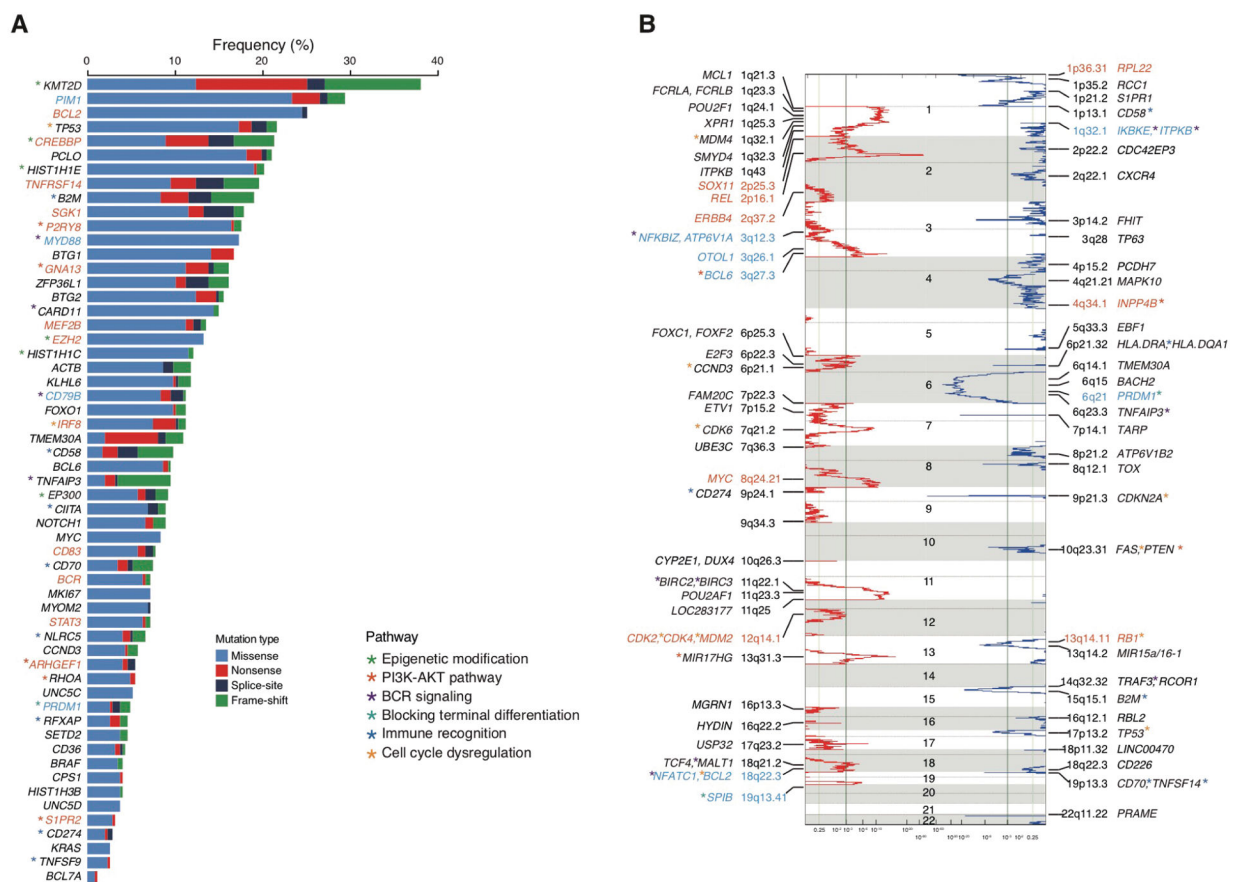
The Fisher's exact test was used when comparing two categorical data. For the comparison of two continuous variables, these data were tested by Wilcoxon rank-sum test, unless otherwise noted. Multiple testing corrections were performed, where necessary, using the Benjamini-Hochberg procedure. All in vitro studies were conducted at least in triplicate, including biological replicates with three unique CRISPR-mediated frameshift mutations. All quantitative results are presented as the mean with standard deviation. The statistical significance of the differences between cell culture groups was determined using two-tailed Student's *t*-test. Primary cell comparisons were analyzed with two-way repeated measure ANOVA with Bonferroni multiple-comparisons test. Global proteomics differential expression was evaluated using probe-level expression change averaging via the

R Bioconductor package, which ranks peptides of each protein by their *P* value generated by a modified paired Student's *t*-test. The FDR was then calculated by the Benjamini–Hochberg procedure. Protein inference was then assigned using Proteome Discoverer (2.1) using Sequest and Mascot. Xenotransplantation survival curves were compared with Log-rank (Mantel-Cox) tests. All reported *P* values were two-sided, and those <0.05 were considered statistically significant. All statistical analyses were performed using GraphPad Prism Version 7 (GraphPad Software Inc.) and the R software v3.2.3.

Reporting Summary.

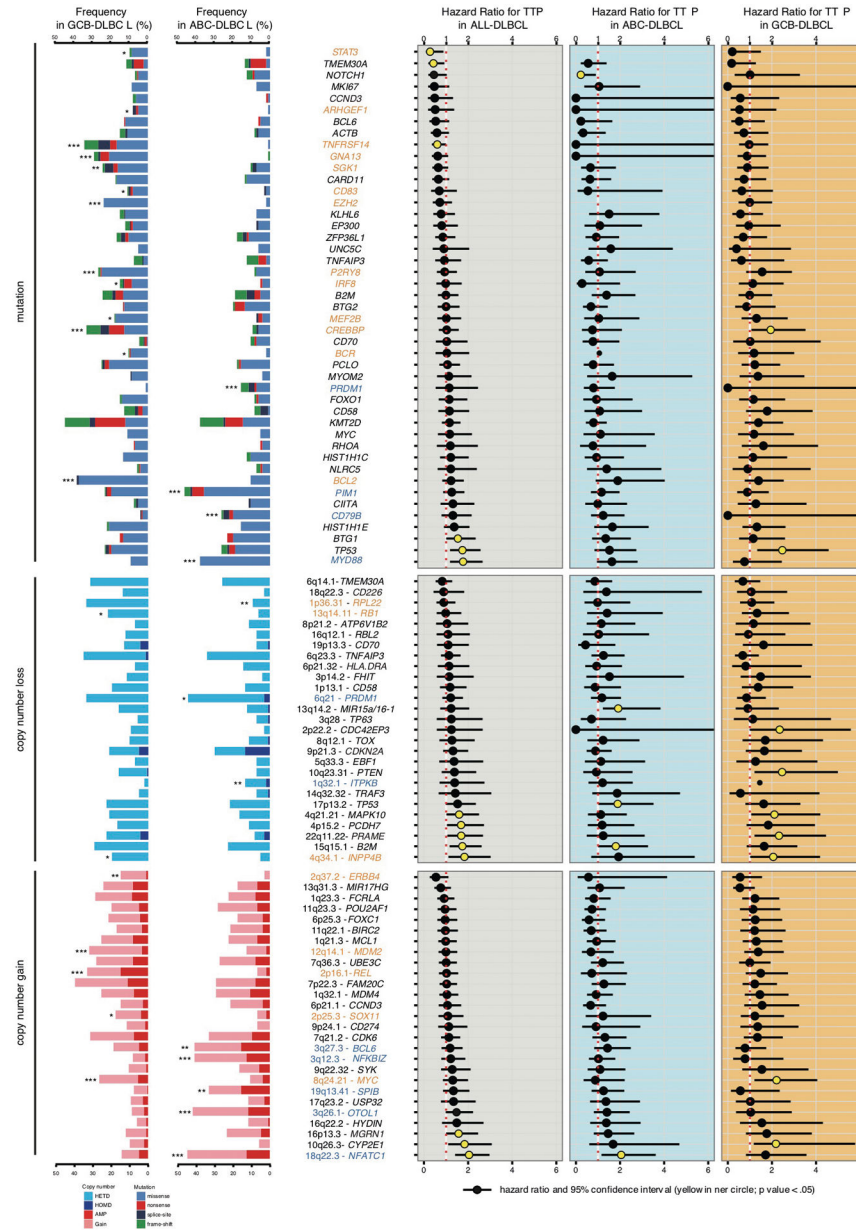
Further information on research design is available in the Nature Research Reporting Summary linked to this article.

Extended Data



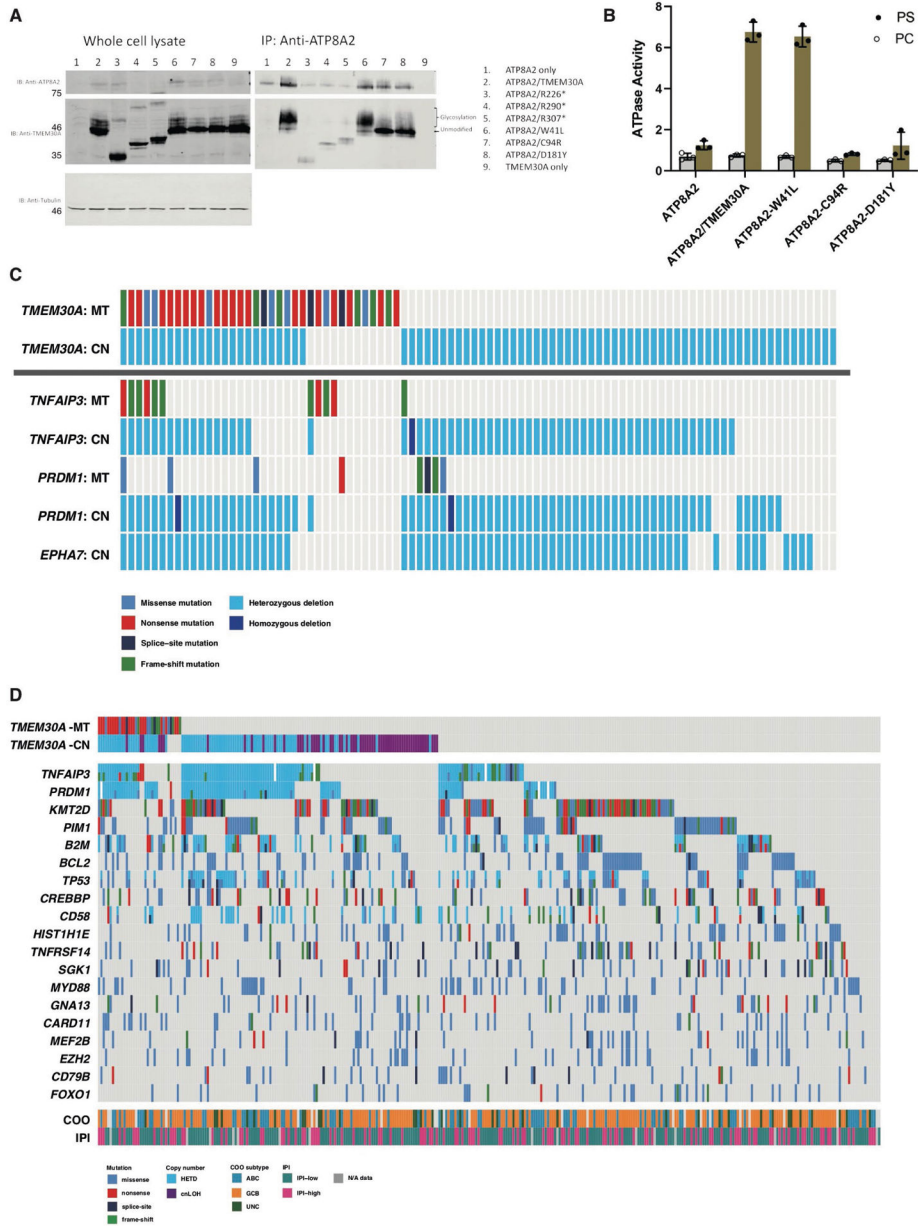
Extended Data Fig. 1 | Recurrent mutation and copy number alterations (CNAs) of DLBCL.
a, Frequencies and type of mutations identified by deep targeted sequencing in 57 recurrently mutated genes in 347 DLBCL tumors. Genes significantly enriched in ABC-DLBCL and GCB-DLBCL are highlighted in blue and orange, respectively. Colored asterisks represent the pathways to which mutations belong. **b**, Significant (*q*-value<0.25) focal amplifications (red) and deletions (blue) identified by GISTIC 2.0 analysis (*n* = 338). Representative genes (functionally known in DLBCL, as well as other cancers) within

significant GISTIC regions are annotated. Genes significantly enriched in ABC-DLBCL and GCB-DLBCL are highlighted in blue and orange, respectively. Colored asterisks represent the pathways to which CNAs belong.



Extended Data Fig. 2 |. Frequencies and prognostic effects of individual genetic alterations. Mutated genes (frequency > 5%) and representative CNAs within GISTIC regions were evaluated. Frequencies of genetic alterations are depicted according to COO subtype. Genes significantly enriched (adjusted p < 0.10, two-sided fisher’s exact test) in ABC-DLBCL (blue) and GCB-DLBCL (orange) are highlighted (left panel). *P < 0.05, **P < 0.01, ***P < 0.001 (adjusted by multiple test). Forest plot summarizes the results of univariate analyses (time-to progression (TTP)) for each genomic alteration, in all DLBCL (grey)-

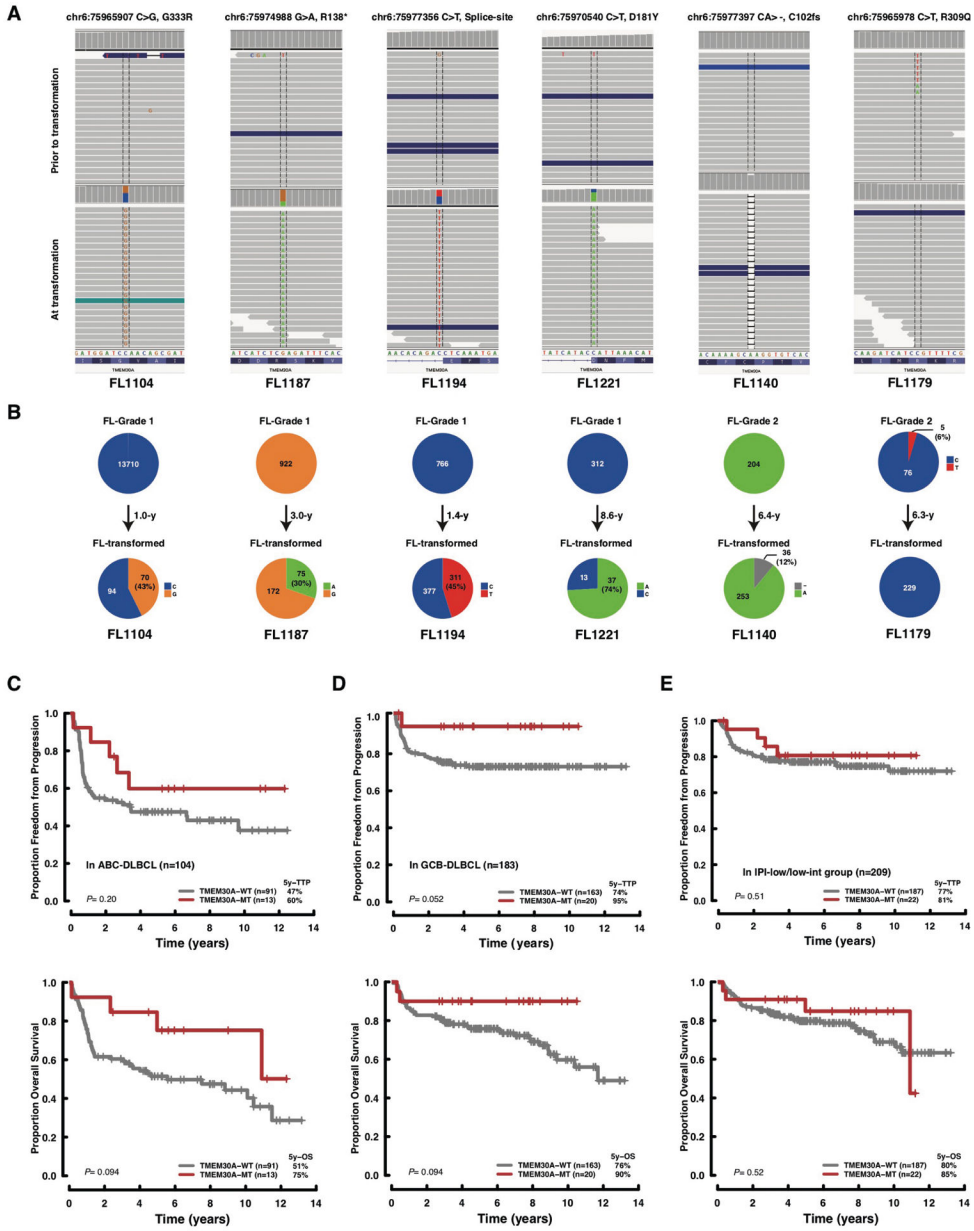
DLBCL (light blue) and in GCB-DLBCL (light-orange). Hazard ratios and 95% confidence intervals are shown. Yellow circles represent significant hazard ratios ($p < 0.05$) (right panel). HETD, heterozygous deletion; HOMD, homozygous deletion; AMP, amplification.



Extended Data Fig. 3 | ATPase activity of *ATP8A2-TMEM30A* variants, and association of recurrent genetic alterations with *TMEM30A* mutation in DLBCL.

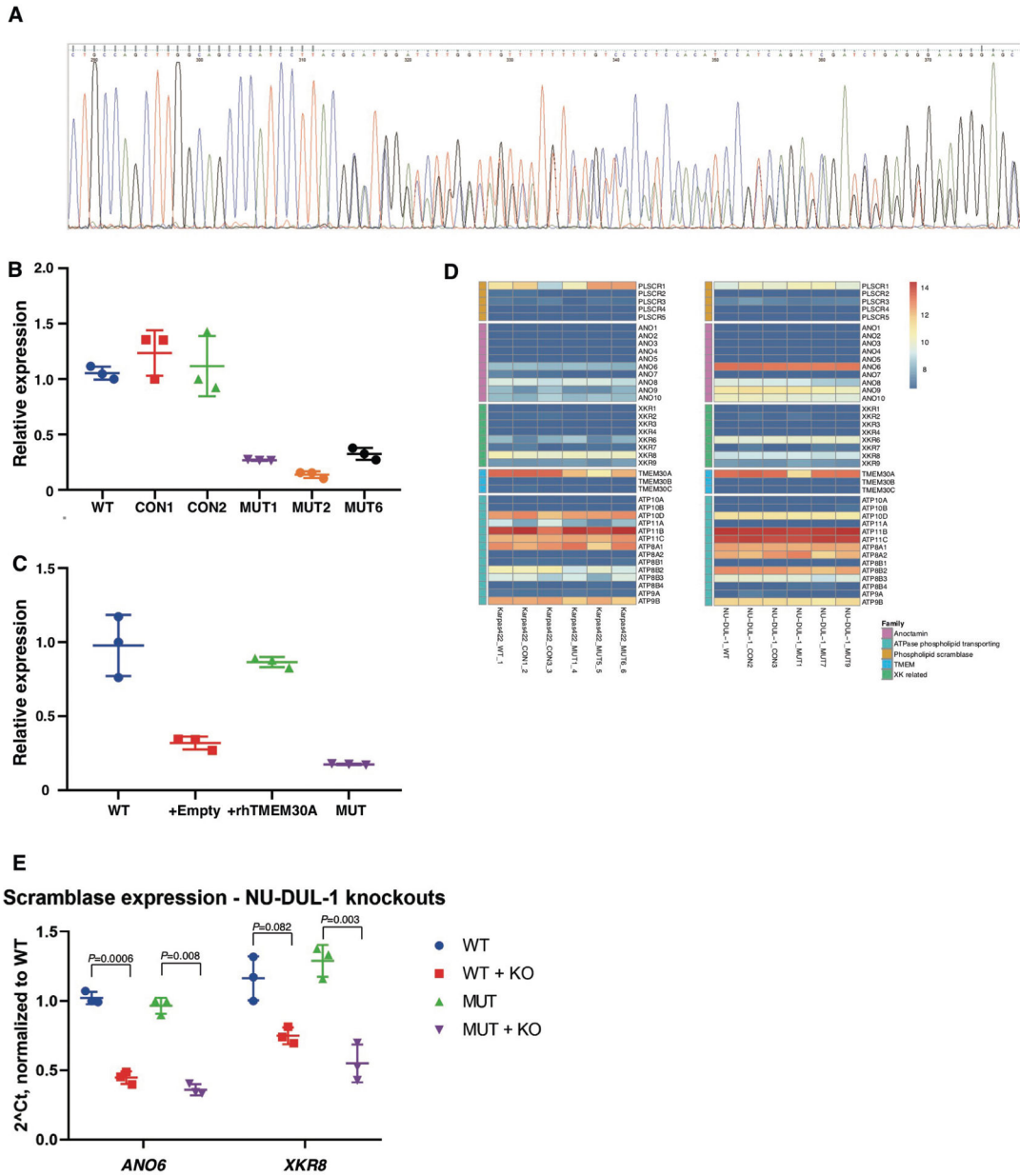
Human *ATP8A2* was expressed with or without human *TMEM30A* or missense mutants in HEK293T cells. **a**, The expressed complex was purified on an *ATP8A2* immunoaffinity column and the input and eluted samples were subjected to SDS gel electrophoresis and western blots were labeled for *ATP8A2* with the Atp6C11 and Cdc50-7F4 antibodies. Cropped images from the same Western blot are shown. Tubulin was detected as a loading control for the input lanes. Independent experiments were repeated twice with

similar results. Source Data Extended Fig. 3. **b**, ATPase activity is measured as nmols of ATP hydrolyzed per 30 min at 37 °C. ATPase activities of the isolated complexes were measured in either 100% dioleoylphosphatidylcholine (PC) or a mixture of 80% dioleoylphosphatidylcholine: 20% dioleoylphosphatidylserine (PS). Samples are: ATP8A2 - expression in the absence of expressed TMEM30A; ATP8A2/WT - co-expression of ATP8A2 with WT- TMEM30A; and ATP8A2/ W41L, ATP8A2/C94R, ATP8A2/D181Y. Graphs represent mean values \pm s.d. ($n = 3$). **c**, Distributions of genetic alterations of *TNFAIP3*, *PRDM1* and *EPHA7* in the patients with *TMEM30A* mutation and deletion. The header includes status of *TMEM30A* mutation and heterozygous deletion. MT; mutation, CN; copy number. **d**, Distributions of recurrent mutation, COO subtypes and IPI groups in *TMEM30A* mutated and wild type DLBCL patients. The header includes the status of *TMEM30A* mutation and CNAs.



Extended Data Fig. 4 | Prevalence and clinical impact of *TMEM30A* mutation.
a, b, Deep targeted sequencing data of transformed FL samples with *TMEM30A* mutation detected at the time of diagnosis or transformation (A). The affected positions of the *TMEM30A* are visualized in an integrative genomic viewer. Variant allelic frequencies are visualized in the pie charts per case (B). Those data demonstrate a fraction of variants at the time of diagnosis (upper row) and transformation (lower row). The number in the pie charts represents the coverage of sequencing. FL1179 exhibited the opposite pattern (T1-positive/T2-negative), however the variant was a missense mutation supported by relatively low coverage (five reads out of 81 (VAF=6%)). **(c-e)** Subtype analysis of survival according to *TMEM30A* genetic alteration. Kaplan Meier curves represent TTP (upper) and OS (bottom)

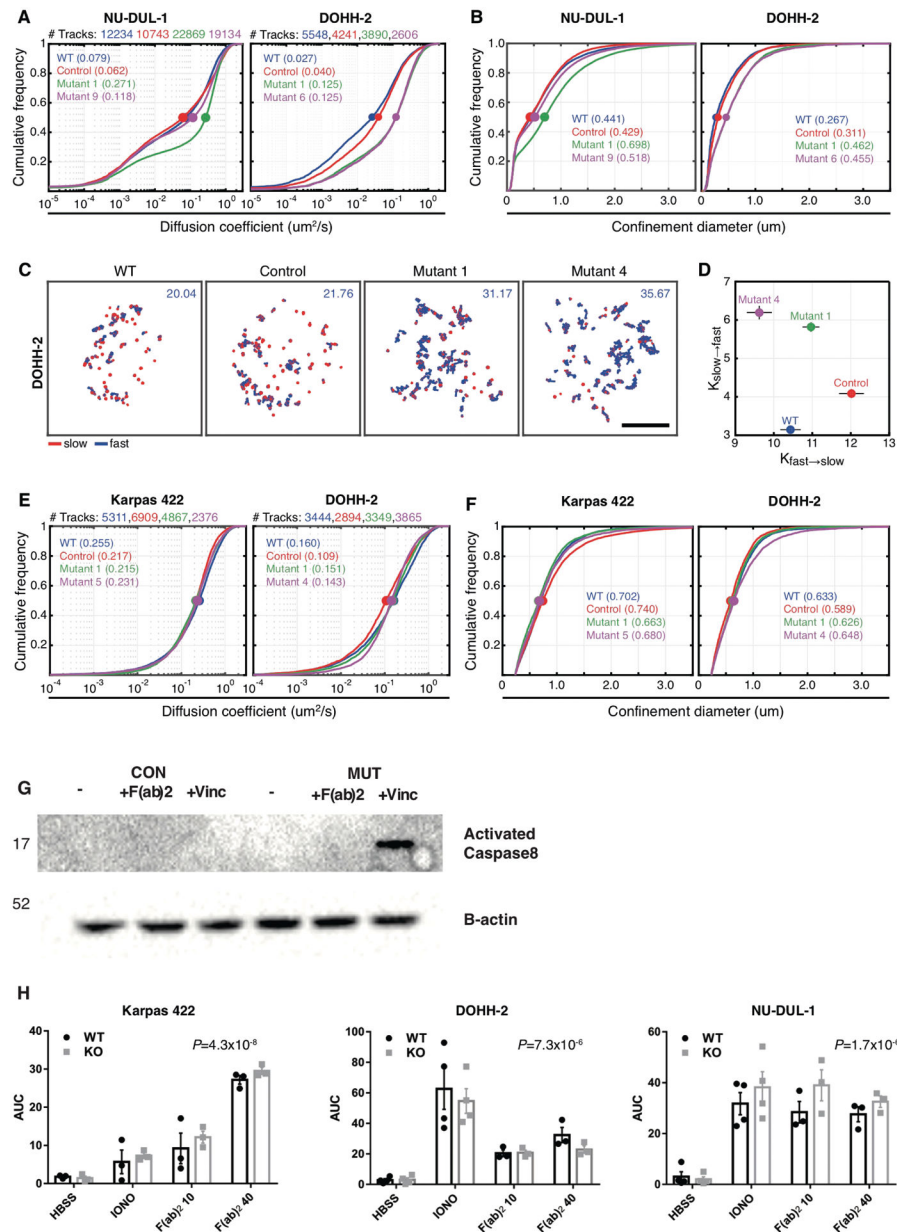
according to *TMEM30A* mutation in ABC-DLBCL (C), in GCB-DLBCL (D) and in IPI-low/low-intermediate group (E). P values were derived from two-sided log-rank test.



Extended Data Fig. 5 |. mRNA expression of *TMEM30A*, related flippases, scramblases and P4-ATPases in in vitro *TMEM30A* knockout cells.

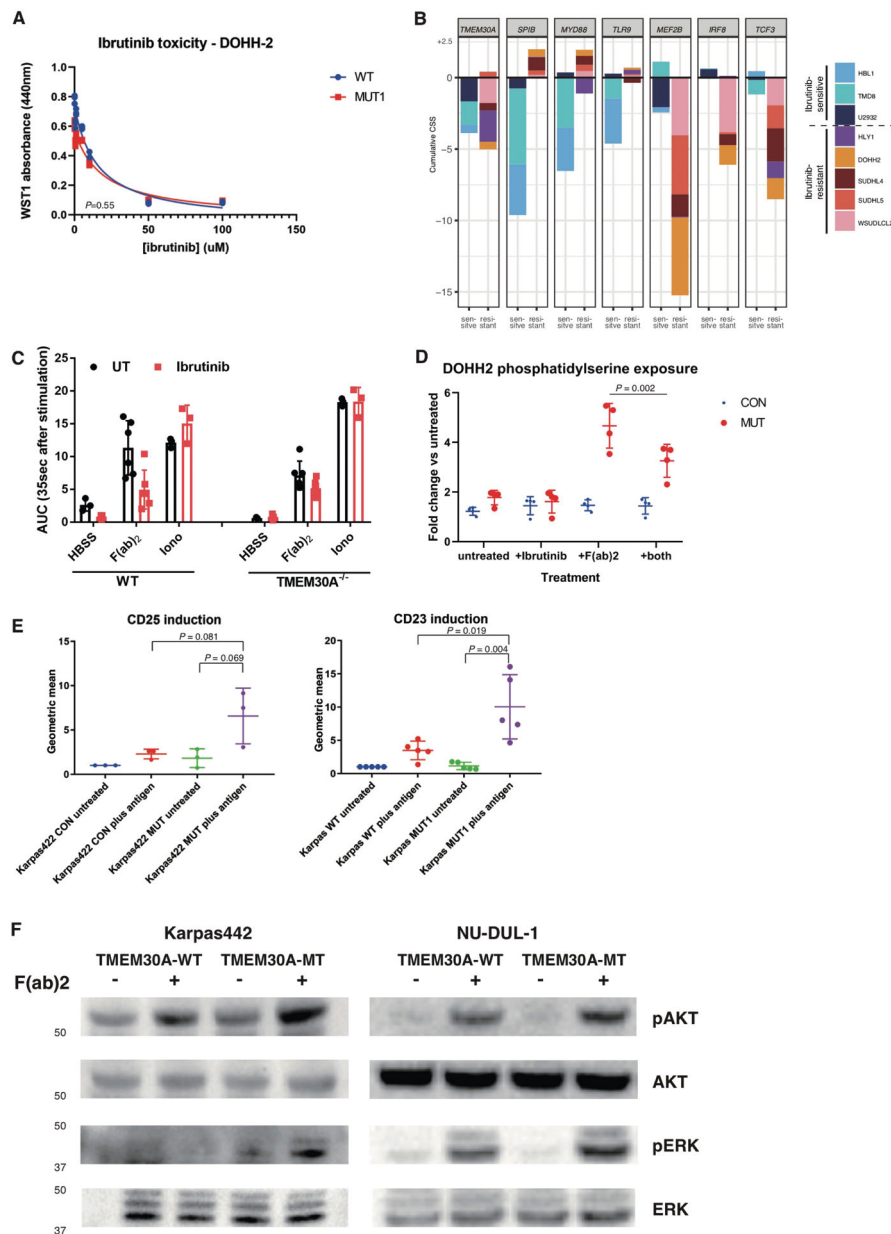
a, A screenshot of a representative sequence trace file of a CRISPR-generated *TMEM30A* frameshift mutation in exon 1 (DOHH-2, MUT1). **b**, *TMEM30A* mRNA expression is reduced in 3 unique bi-allelic frame-shift mutations in Karpas422, compared with parental and single cell enriched controls. mRNA expression is normalized to GAPDH expression. Graphs represent mean values ± s.d. (*n* = 3). **(c)** mRNA expression of *TMEM30A* is ‘rescued’ in one unique bi-allelic *TMEM30A* mutant, by ectopically expressing a stable insertion of a *TMEM30A* cDNA. Graphs represent mean values ± s.d. (*n* = 3). **d**, mRNA

levels of different scramblases (PLSCR1-5; ANO1-10, XKR1-9), flippases (*TMEM30A-C*) and P4-ATPases in Karpas422 (left panel) and NUDUL-1 (right panel) native (WT, CON) and *TMEM30A*^{-/-} (MUT) cell lines. Protein family members are categorized, and the heat map values show log-normalized expression by RNA-seq. **e**, *XKR8* and *ANO6* mRNA expression is reduced in 3 unique bi-allelic (*XKR8*) and mono-allelic (*ANO6*) frame-shift mutations in *TMEM30A*^{-/-} and wildtype controls. mRNA expression is normalized to GAPDH expression. Graphs represent mean values \pm s.d. ($n = 3$). All P values are based on a paired two-tailed Student's t test.



Extended Data Fig. 6 | BCR activation, mobility and clustering in NU-DUL-1 and DOHH-2 as measured by single particle tracking analysis.

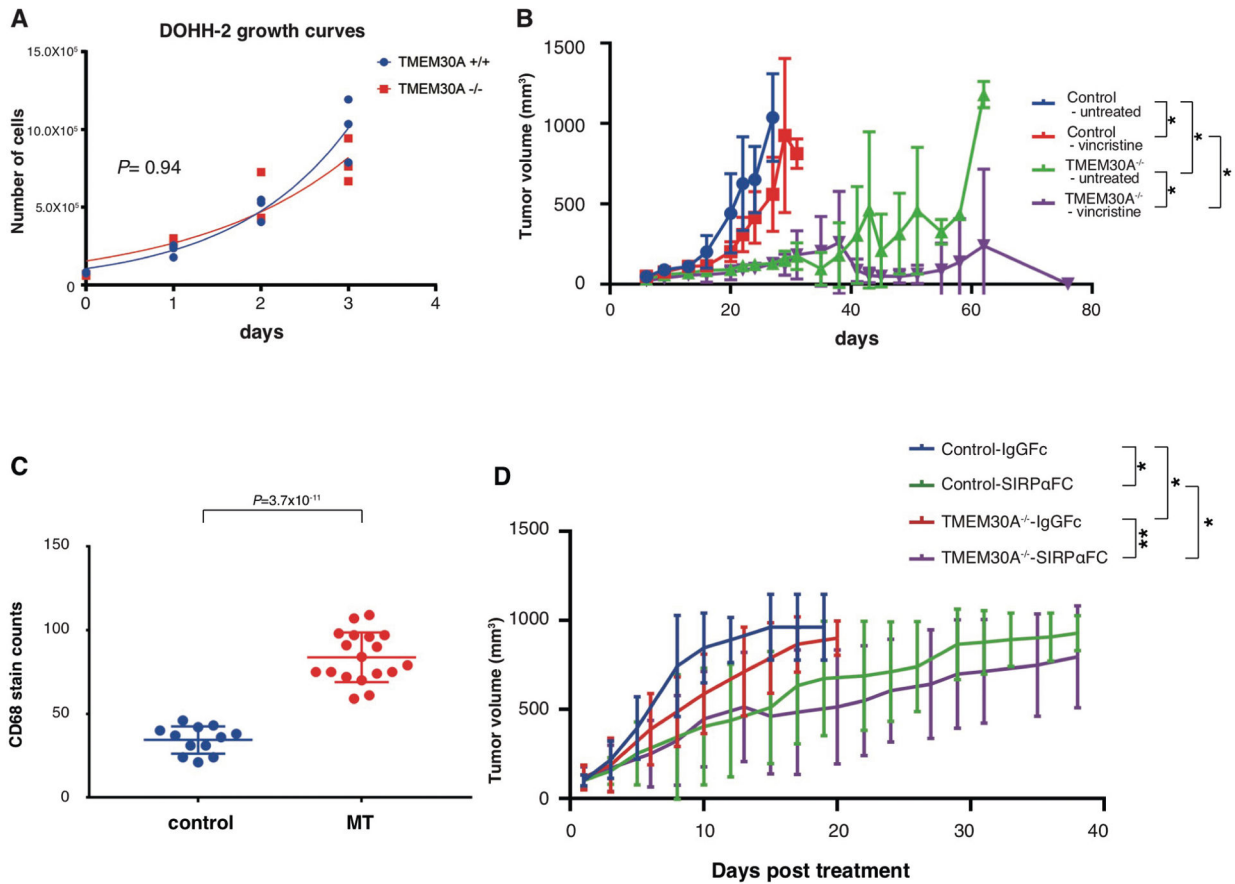
a, Single-state diffusion coefficients and **b**, confinement-diameters are shown for both cell lines, and **c**, BCR tracks and **d**, transition rates are measured for DOHH-2. The dots indicate median values; lines indicate 95% confidence intervals (($n=3$, DOHH-2) ($n=2$, NU-DUL-1). (E-F) TMEM30A mutation does not alter CD19 diffusion and confinement diameters. Cells were labelled with anti-CD19 Fab-Cy3, settled onto poly-L-lysine coated coverslips and imaged for 10 s at 33 Hz. **e**, Single-state diffusion coefficients were calculated for all tracks and cumulative frequency curves are shown. The dots on the curves indicate the median values and are reported in brackets. Total number of tracks analyzed in each condition is shown above the plot. **f** The cumulative frequency curves of the confinement-diameters with the median values (dots on the curves) indicated in brackets. **g**, BCR activation of DLBCL cell lines following incubation with F(ab)₂ fragments does not lead to an increase in apoptotic signaling through caspase 3 activation, measurable by western blot analysis. Cells (Karpas422) pretreated with vincristine were included as a positive control. Cropped images from the same Western blot are shown. B-actin is used as a loading control. Experiments were repeated independently three times with similar results. Source Data Extended Fig. 6. **h**, Ca²⁺ mobilization was measured in wild type (WT) and TMEM30A^{-/-} NU-DUL-1, DOHH-2 and Karpas422 cells, following HBSS, F(ab)₂ addition (10 and 40 μg/ml) and ionomycin. Graphs represent mean values ± s.d. ($n=3$). Significance is evaluated using one-way ANOVA.



Extended Data Fig. 7 | B-cell signalling following ibrutinib treatment in B cell lymphoma lines with TMEM30A loss-of-function mutation.

a, DOHH-2 toxicity of ibrutinib after 24 hours incubation. Toxicity between wildtype (red line) and TMEM30A^{-/-} (blue line) was measured by WST1 colorimetric assays (mean of triplicate is shown). P value is based on an unpaired two-tailed Student's t test. **b**, Comparisons of CRISPR screen score (CSS) between ibrutinib-sensitive vs -resistance cell lines in publicly available dataset. CSS was defined as the number of standard deviations away from the average effect of inactivating a gene. The differences of CSS in TMEM30A-targeting was not observed, while there are strong differences of CSS in other genes known to be involved in the determination of ibrutinib-sensitivity (for example *MYD88*, *MEF2B* etc) **c**, Ca²⁺ mobilization was measured in wildtype (WT) and TMEM30A^{-/-} DOHH-2 cells, following HBSS, F(ab)₂ and ionomycin, with or without (UT) overnight pretreatment

with ibrutinib. Graphs represent mean values \pm s.d. ($n = 3$ (HBSS), $n = 6$ (F(ab)₂), $n = 3$ (iono)). **d**, Effects of ibrutinib pretreatment on F(ab)₂ fragment PS exposure in DOHH-2 TMEM30A^{-/-} and native control, measured by annexin V-APC binding. Addition of ibrutinib to F(ab)₂ fragment stimulated TMEM30A^{-/-} cells shows a significant reduction in PS exposure. Graphs represent mean values \pm s.d. ($n = 4$). P value is based on a two-way ANOVA test. **e**, Induction of CD25 (left panel) and CD23 (right panel) following BCR activation in Karpas422 cell lines with (MUT) or without (CON) a biallelic loss-of function in TMEM30A. Surface marker expression was measured by flow cytometry, using protein specific antibodies. Graphs represent mean values \pm s.d. ($n = 3$ (CD25), $n = 5$ (CD23)). P value is based on an unpaired two-tailed Student's t test. **f**, Activation by phosphorylation of AKT and ERK1/2 in Karpas422 and NU-DUL-1 native and TMEM30A^{-/-} cells, detected by Western blot analysis, following overnight F(ab)₂ fragment stimulation. Cropped images from the same Western blot are shown. Unphosphorylated AKT or ERK1/2 is used as a loading control. Experiments were repeated independently three times with similar results. Source Data Extended Fig. 7.



Extended Data Fig. 8 | TMEM30A loss-of-function enhanced survival and increased macrophage engulfment following vincristine and CD47 blockade treatment.

a, Proliferation rates of native (blue line) and TMEM30A^{-/-} (red line) DOHH-2 cells, measured over 3 days by WST1 absorbance. Cell numbers were extrapolated from a WST1 standard curve, using known quantities of DOHH-2. P value is based on an unpaired

two-tailed Student's t test. **b**, Xenotransplantation models of DOHH-2 cells with parental or TMEM30A^{-/-} subcutaneously injected into NSG mice (5 per group). Vincristine treatment (0.1 mg/kg) or saline control (untreated) was administered when tumor volumes per group reached 100 mm³. Line graphs show tumor growth (mm³) over time (days). Graphs represent mean values ± s.d. P values are based on a paired two-tailed Student's t test. *P<0.05. **c**, The comparison of macrophage counts in tumor tissue from untreated DOHH-2 xenotransplantation models, visualized by CD68 antibody with H&E counter staining, per tissue within randomly selected 400x high power field regions per tumor from 3 separate mice per group. Graphs represent mean values ± s.d. (*n* = 12 (control), *n* = 18 (MT)). P values are based on a paired two-tailed Student's t test. **d**, Xenotransplantation models of DOHH-2 cells with parental or TMEM30A^{-/-} subcutaneously injected into NSG mice (10 per group). TTI-621 treatment (10 mg/kg) or TTI-402 (6.67 mg/kg) was initiated when tumor volumes per group reached 100 mm³. Normalized mean tumor growth (mm³) over time (days) starting at injection time. Graphs represent mean values ± s.d. P values are based on a paired two-tailed Student's t test. *P<0.05, **P<0.01.

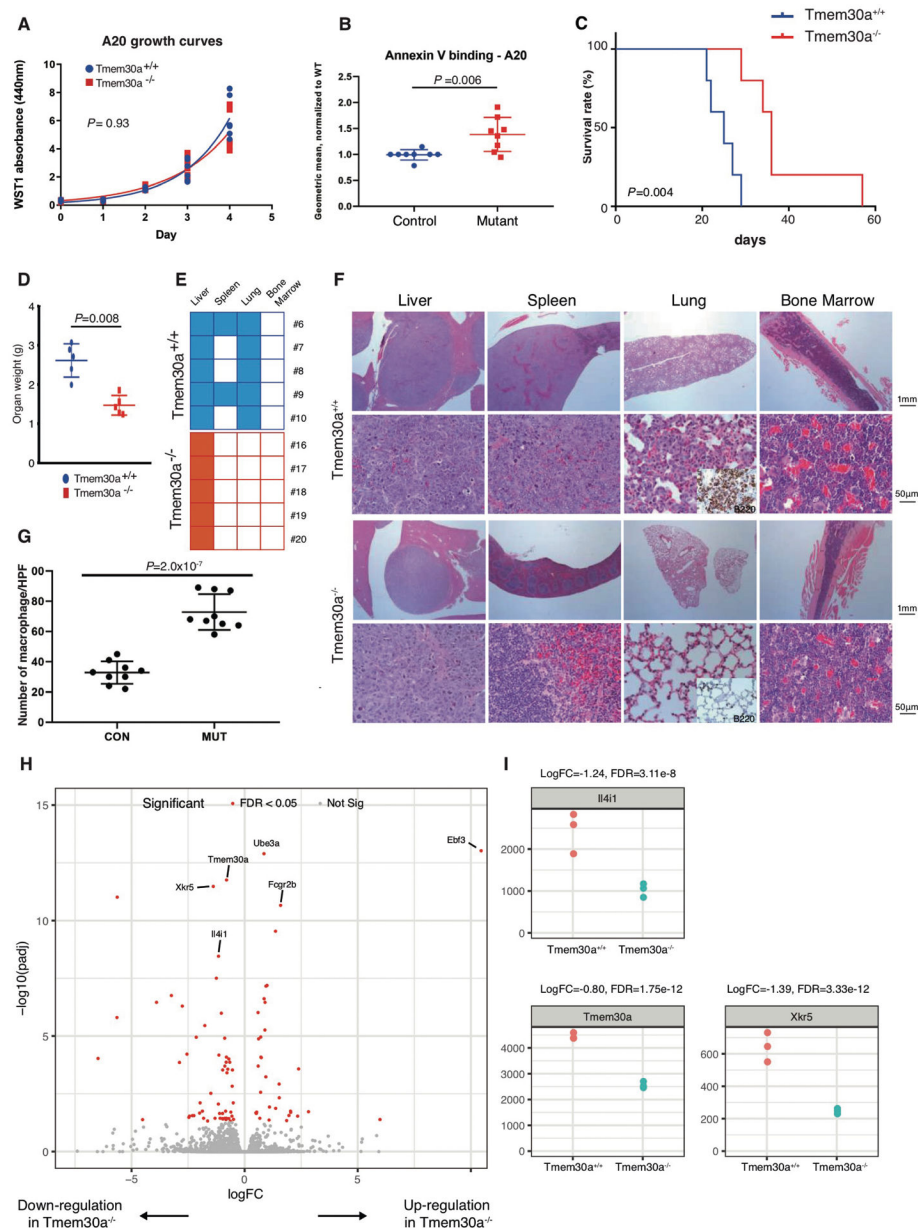
two-tailed Student's t test. **b**, Xenotransplantation models of DOHH-2 cells with parental or TMEM30A^{-/-} subcutaneously injected into NSG mice (5 per group). Vincristine treatment (0.1 mg/kg) or saline control (untreated) was administered when tumor volumes per group reached 100 mm³. Line graphs show tumor growth (mm³) over time (days). Graphs represent mean values ± s.d. P values are based on a paired two-tailed Student's t test. *P<0.05. **c**, The comparison of macrophage counts in tumor tissue from untreated DOHH-2 xenotransplantation models, visualized by CD68 antibody with H&E counter staining, per tissue within randomly selected 400x high power field regions per tumor from 3 separate mice per group. Graphs represent mean values ± s.d. (*n* = 12 (control), *n* = 18 (MT)). P values are based on a paired two-tailed Student's t test. **d**, Xenotransplantation models of DOHH-2 cells with parental or TMEM30A^{-/-} subcutaneously injected into NSG mice (10 per group). TTI-621 treatment (10 mg/kg) or TTI-402 (6.67 mg/kg) was initiated when tumor volumes per group reached 100 mm³. Normalized mean tumor growth (mm³) over time (days) starting at injection time. Graphs represent mean values ± s.d. P values are based on a paired two-tailed Student's t test. *P<0.05, **P<0.01.

Author Manuscript

Author Manuscript

Author Manuscript

Author Manuscript



Extended Data Fig. 9 | *In vitro* and *in vivo* macrophage association and infiltration of A20 Tmem30A loss-of-function in Balb/c.

a, Syngeneic mouse modeling in Balb/c mice with $Tmem30a^{-/-}$ or wildtype ($Tmem30a^{+/+}$) A20 cells. Proliferation rates of $Tmem30a^{-/-}$ (red line) and wildtype (blue line) A20 cells, measurable over 4 days by WST1 absorbance. P values are based on an unpaired two-tailed Student's t test ($n = 6$). b, Comparison of PS exposure in $Tmem30a^{-/-}$ or wildtype A20 cells, measured by annexin V-APC binding. Graphs represent mean values \pm s.d. ($n = 8$) P values are based on an unpaired two-tailed Student's t test. c, Syngeneic mouse models of A20 cells with wildtype or $Tmem30a^{-/-}$ cells intravenously injected into Balb/c mice (5 per group). Kaplan-Meier plots show overall survival of Balb/c inoculated mice. P value is based on a Mantel-Cox test. d, Organ weight of livers from Balb/c mice intravenously injected with $Tmem30a^{-/-}$ or wildtype cells. All mice were sacked at the first presentation

of abdominal distention in the control group ('early sac'). Graphs represent mean values \pm s.d. ($n = 5$). P values are based on an unpaired two-tailed Student's t test. (E-F) Observation of tumor infiltrate in mice injected with *Tmem30a*^{-/-} or wildtype cells at early sac. e, Blue or red filled column indicates positive tumor infiltration in wildtype or *Tmem30a*^{-/-} cells, with blank indicating no tumor infiltration. f, H&E staining of each organ at early sac (liver, spleen, lung, and bone marrow) with inset of B220 IHC in the lung specimen. N = 5 mice per group. g, The comparison of macrophage counts in tumor tissue from subcutaneous injected A20 *Tmem30a*^{-/-} and wildtype cells, visualized by F4/80 antibody with H&E counter staining, per tissue within 3 randomly selected 400x high power field regions per tumor from 3 separate mice per group. Graphs represent mean values \pm s.d. P values are based on an unpaired two-tailed Student's t test. h, i, Comparison of gene expression between tumor tissue from *Tmem30a*^{-/-} and control injection groups. (N = 3 RNA samples from each mouse group). To generate P values (padj/FDR), we used a Wald test of the coefficients fit with a negative binomial GLM. The P values are two-sided and have all been adjusted for multiple comparisons using the Benjamini-Hochberg method. (H) Volcano plot of difference in gene expression between *Tmem30a*^{-/-} and control groups (x-axis; log₂ fold change of difference) and significance (y-axis). Red dots show the genes with significant difference (FDR < 0.05). (I) Dot plots show gene expression (FPKM) of *Ii4i1*, *Tmem30a* and *Xkr5* between *Tmem30a*^{-/-} and control groups.

Supplementary Material

Refer to Web version on PubMed Central for supplementary material.

Authors

Daisuke Ennishi^{1,2,17}, Shannon Healy^{1,17}, Ali Bashashati^{3,17}, Saeed Saberi³, Christoffer Hother¹, Anja Mottok^{1,4}, Fong Chun Chan^{1,5}, Lauren Chong¹, Libin Abraham⁶, Robert Kridel¹, Merrill Boyle¹, Barbara Meissner¹, Tomohiro Aoki¹, Katsuyoshi Takata¹, Bruce W. Woolcock¹, Elena Viganò¹, Michael Gold⁶, Laurie L. Molday⁷, Robert S. Molday⁷, Adele Telenius¹, Michael Y. Li¹, Nicole Wretham⁸, Nancy Dos Santos⁸, Mark Wong⁹, Natasja N. Viller⁹, Robert A. Uger⁹, Gerben Duns¹, Abigail Baticados¹, Angel Madero¹, Brianna N. Bristow¹, Pedro Farinha¹, Graham W. Slack¹, Susana Ben-Neriah¹, Daniel Lai³, Allen W. Zhang³, Sohrab Salehi³, Hennady P. Shulha¹, Derek S. Chiu¹⁰, Sara Mostafavi^{10,11}, Alina S. Gerrie¹, Da Wei Huang¹², Christopher Rushton¹³, Diego Villa¹, Laurie H. Sehn¹, Kerry J. Savage¹, Andrew J. Mungall¹⁴, Andrew P. Weng¹⁵, Marcel B. Bally⁸, Ryan D. Morin^{13,14}, Gabriela V. Cohen Freue¹⁰, Louis M. Staudt¹², Joseph M. Connors¹, Marco A. Marra^{11,14}, Sohrab P. Shah^{3,14,16,18}, Randy D. Gascoyne^{1,16,18}, David W. Scott^{1,18}, Christian Steidl^{1,16,18}

Affiliations

¹Centre for Lymphoid Cancer, British Columbia Cancer, Vancouver, British Columbia, Canada.

²Department of Hematology and Oncology, Okayama University Hospital, Okayama, Japan.

³Molecular Oncology, British Columbia Cancer, Vancouver, British Columbia, Canada.

⁴Institute of Human Genetics, Ulm University and Ulm University Medical Center, Ulm, Germany.

⁵Bioinformatics Graduate Program, University of British Columbia, Vancouver, British Columbia, Canada.

⁶Department of Microbiology and Immunology, University of British Columbia, Vancouver, British Columbia, Canada.

⁷Department of Biochemistry and Molecular Biology, University of British Columbia, Vancouver, British Columbia, Canada.

⁸Department of Experimental Therapeutics, British Columbia Cancer, Vancouver, British Columbia, Canada.

⁹Trillium Therapeutics Inc., Mississauga, Ontario, Canada.

¹⁰Department of Statistics, University of British Columbia, Vancouver, British Columbia, Canada.

¹¹Department of Medical Genetics, University of British Columbia, Vancouver, British Columbia, Canada.

¹²Lymphoid Malignancies Branch, National Cancer Institute, National Institutes of Health, Bethesda, MD, USA.

¹³Department of Molecular Biology and Biochemistry, Simon Fraser University, Burnaby, British Columbia, Canada.

¹⁴Canada's Michael Smith Genome Sciences Centre, British Columbia Cancer, Vancouver, British Columbia, Canada.

¹⁵Terry Fox Laboratory, British Columbia Cancer, Vancouver, British Columbia, Canada.

¹⁶Department of Pathology and Laboratory Medicine, University of British Columbia, Vancouver, British Columbia, Canada.

¹⁷These authors contributed equally: Daisuke Ennishi, Shannon Healy, Ali Bashashati.

¹⁸These authors jointly supervised this work: Sohrab P. Shah, Randy D. Gascoyne, David W. Scott, Christian Steidl.

Acknowledgements

This study was supported by a Program Project Grant from the Terry Fox Research Institute (R.D.G, grant no. 1023; C.S., grant no. 1061), a Large Scale Applied Research Project (LSARP) from Genome Canada (C.S., grant no. 13124), Genome British Columbia (C.S., 271LYM), Canadian Institutes of Health Research (CIHR) (C.S., GP1-155873) and the British Columbia Cancer Foundation (BCCF). D.E. was supported by fellowships from the

Michael Smith Foundation for Health Research (MSFHR), Canadian Institutes of Health Research (CIHR) and Japanese Society for The Promotion of Science. D.W.S. is supported by the British Columbia Cancer Foundation (BCCF) and the Michael Smith Foundation for Health Research (MSFHR). J.M.C. was the Clinical Director of the British Columbia Cancer Agency Centre for Lymphoid Cancer and received research funding support from the Terry Fox Research Institute, Genome Canada, Genome British Columbia, CIHR and the BCCF. C.H. was supported by the Alfred Benzon foundation. A.M. is supported by fellowships from the Mildred-Scheel-Cancer-Foundation (German Cancer Aid), the MSFHR and Lymphoma Canada. E.V. is supported by a fellowship from the Michael Smith Foundation for Health Research. G.V.C.F is supported by an NSERC Discovery grant. R.D.M. is funded by a CIHR New Investigator Award. M.A.M. is UBC Canada Research Chair in Genome Science and is pleased to acknowledge support from CIHR (FDN-143288) and the Terry Fox Research Institute. S.P.S. holds the Canada Research Chair in Computational Cancer Genomics, is a MSFHR scholar, holds a CIHR Foundation grant and acknowledges support from the BCCF. T.A. was supported by the Japanese Society for the Promotion of Science and the Uehara Memorial Foundation. T.A. received research funding support from The Kanae Foundation for the Promotion of Medical Science. L.A., as well as the experiments carried out by L.A., were supported by CIHR grant PJT-152946 (to M.R.G.). R.S.M holds a Canada Research Chair in Vision and Macular Degeneration and acknowledges support from CIHR (PJT-148649). K.T. was supported by fellowships from the Uehara Memorial Foundation. We thank E. Toombs for assistance in performing research, analyzing and interpreting data.

Competing interests

D.W.S., J.M.C. and R.D.G. are inventors on a patent held by the National Cancer Institute that has been licensed by NanoString Technologies. C.S. has performed consultancy for Seattle Genetics, Curis Inc., Roche, AbbVie, Juno Therapeutics and Bayer, and has received research funding from Bristol-Myers Squibb and Trillium Therapeutics Inc. D.W.S. has performed consultancy for Janssen and Celgene and has received research funding from Roche/Genentech, Janssen and NanoString Technologies. R.D.G. has performed consultancy for Celgene. R.K. received travel support from Roche. D.V., A.S.G, K.J.S., J.M.C., L.H.S. and D.W.S. received institutional research funding from Roche. L.H.S. has performed consultancy and received honoraria from Amgen, Abbvie, Apobiologix, Celgene, Lundbeck, Janssen, Karyopharm, TG Therapeutics, Roche/Genentech, Teva and Takeda. K.J.S. received honoraria and provided consultancy to Bristol-Myers Squibb, Merck, Takeda, Verastem and Servier. A.S.G. received honoraria and provided consultancy to Janssen, AbbVie and Seattle Genetics. D.V. received honoraria from and participated in advisory boards for: Roche, Abbvie, Celgene, Seattle Genetics, Lundbeck, AstraZeneca, Nanostring, Janssen and Gilead.

Data availability

Full data, including patient characteristics, mutation data and experimental data, are provided as Supplementary Tables 2, 3, 8 and 9) and in our previous paper⁴⁹. The raw sequencing data have been deposited in the European Genome-phenome Archive (EGA) under accession number EGAS00001002657. Source data for Fig. 5b and Extended Data Figs. 3a, 6g and 7f are presented with the paper.

References

1. Swerdlow SH et al. The 2016 revision of the World Health Organization (WHO) classification of lymphoid neoplasms. *Blood* 127, 2375–2390 (2016). [PubMed: 26980727]
2. Coiffier B et al. CHOP chemotherapy plus rituximab compared with CHOP alone in elderly patients with diffuse large-B-cell lymphoma. *N. Engl. J. Med* 346, 235–242 (2002). [PubMed: 11807147]
3. Sehn LH et al. Introduction of combined CHOP plus rituximab therapy dramatically improved outcome of diffuse large B-cell lymphoma in British Columbia. *J. Clin. Oncol* 23, 5027–5033 (2005). [PubMed: 15955905]
4. Alizadeh AA et al. Distinct types of diffuse large B-cell lymphoma identified by gene expression profiling. *Nature* 403, 503–511 (2000). [PubMed: 10676951]
5. Rosenwald A et al. The use of molecular profiling to predict survival after chemotherapy for diffuse large-B-cell lymphoma. *N. Engl. J. Med* 346, 1937–1947 (2002). [PubMed: 12075054]
6. Shipp MA et al. Diffuse large B-cell lymphoma outcome prediction by gene-expression profiling and supervised machine learning. *Nat. Med* 8, 68–74 (2002). [PubMed: 11786909]
7. Morin RD et al. Frequent mutation of histone-modifying genes in non-Hodgkin lymphoma. *Nature* 476, 298–303 (2011). [PubMed: 21796119]

8. Pasqualucci L et al. Analysis of the coding genome of diffuse large B-cell lymphoma. *Nat. Genet* 43, 830–837 (2011). [PubMed: 21804550]
9. Lohr J Get al. Discovery and prioritization of somatic mutations in diffuse large B-cell lymphoma (DLBCL) by whole-exome sequencing. *Proc. Natl Acad. Sci. USA* 109, 3879–3884 (2012). [PubMed: 22343534]
10. Zhang J et al. Genetic heterogeneity of diffuse large B-cell lymphoma. *Proc. Natl Acad. Sci. USA* 110, 1398–1403 (2013). [PubMed: 23292937]
11. Reddy A et al. Genetic and functional drivers of diffuse large B cell lymphoma. *Cell*. 171, 481–494.e15 (2017). [PubMed: 28985567]
12. Chapuy B et al. Molecular subtypes of diffuse large B cell lymphoma are associated with distinct pathogenic mechanisms and outcomes. *Nat. Med* 24, 679–690 (2018). [PubMed: 29713087]
13. Schmitz R et al. Genetics and pathogenesis of diffuse large B-cell lymphoma. *N. Engl. J. Med* 378, 1396–1407 (2018). [PubMed: 29641966]
14. Ding J et al. Systematic analysis of somatic mutations impacting gene expression in 12 tumour types. *Nat. Commun* 6, 8554 (2015). [PubMed: 26436532]
15. Lopez-Marques RL, Theorin L, Palmgren MG & Pomorski TG P4-ATPases: lipid flippases in cell membranes. *Pflugers Arch. Eur. J. Physiol* 466, 1227–1240 (2014). [PubMed: 24077738]
16. van der Mark VA, Oude Elferink RPJ & Paulusma CC P4 ATPases: flippases in health and disease. *Int. J. Mol. Sci* 14, 7897–7922 (2013). [PubMed: 23579954]
17. Coleman JA & Molday RS Critical role of the β -subunit CDC50A in the stable expression, assembly, subcellular localization, and lipid transport activity of the P₄-ATPase ATP8A2. *J. Biol. Chem* 286, 17205–17216 (2011). [PubMed: 21454556]
18. Puts CF & Holthuis JCM Mechanism and significance of P4 ATPase catalyzed lipid transport: lessons from a Na⁺/K⁺-pump. *Biochim. Biophys. Acta - Mol. Cell Biol. Lipids* 1791, 603–611 (2009).
19. Segawa K, Kurata S & Nagata S The CDC50A extracellular domain is required for forming a functional complex with and chaperoning phospholipid flippases to the plasma membrane. *J. Biol. Chem* 293, 2172–2182 (2018). [PubMed: 29276178]
20. Kridel R et al. Histological transformation and progression in follicular lymphoma: a clonal evolution study. *PLoS Med.* 13, e1002197 (2016). [PubMed: 27959929]
21. Segawa K et al. Caspase-mediated cleavage of phospholipid flippase for apoptotic phosphatidylserine exposure. *Science* 344, 1164–1168 (2014). [PubMed: 24904167]
22. Treanor B B-cell receptor: from resting state to activate. *Immunology* 136, 21–27 (2012). [PubMed: 22269039]
23. Treanor B et al. The membrane skeleton controls diffusion dynamics and signaling through the B cell receptor. *Immunity* 32, 187–199 (2010). [PubMed: 20171124]
24. Mattila P K et al. The actin and tetraspanin networks organize receptor nanoclusters to regulate B cell receptor-mediated signaling. *Immunity* 38, 461–474 (2013). [PubMed: 23499492]
25. Mattila P K, Batista F D & Treanor B Dynamics of the actin cytoskeleton mediates receptor cross talk: an emerging concept in tuning receptor signaling. *J. Cell Biol* 212, 267–280 (2016). [PubMed: 26833785]
26. Freeman S A et al. Toll-like receptor ligands sensitize B-cell receptor signalling by reducing actin-dependent spatial confinement of the receptor. *Nat. Commun* 6, 6168 (2015). [PubMed: 25644899]
27. Das R, Cairo C W & Coombs D A hidden Markov model for single particle tracks quantifies dynamic interactions between LFA-1 and the actin cytoskeleton. *PLoS Comput. Biol* 5, e1000556 (2009). [PubMed: 19893741]
28. Phelan J D et al. A multiprotein supercomplex controlling oncogenic signalling in lymphoma. *Nature* 560, 387–391 (2018). [PubMed: 29925955]
29. Suzuki J, Umeda M, Sims P J & Nagata S Calcium-dependent phospholipid scrambling by TMEM16F. *Nature* 468, 834–838 (2010). [PubMed: 21107324]
30. Hankins H M, Baldrige R D, Xu P & Graham T R Role of flippases, scramblases and transfer proteins in phosphatidylserine subcellular distribution. *Traffic* 16, 35–47 (2015). [PubMed: 25284293]

31. Birge RB et al. Phosphatidylserine is a global immunosuppressive signal in efferocytosis, infectious disease, and cancer. *Cell Death Differ.* 23, 962–978 (2016). [PubMed: 26915293]
32. Nagata S, Suzuki J, Segawa K & Fujii T Exposure of phosphatidylserine on the cell surface. *Cell Death Differ.* 23, 952–961 (2016). [PubMed: 26891692]
33. Segawa K & Nagata S An apoptotic ‘eat me’ signal: phosphatidylserine exposure. *Trends Cell Biol.* 25, 639–650 (2015). [PubMed: 26437594]
34. Suzuki J, Imanishi E & Nagata S Xkr8 phospholipid scrambling complex in apoptotic phosphatidylserine exposure. *Proc. Natl Acad. Sci. USA* 113, 9509–9514 (2016). [PubMed: 27503893]
35. Suzuki J, Denning DP, Imanishi E, Horvitz HR & Nagata S Xk-related protein 8 and CED-8 promote phosphatidylserine exposure in apoptotic cells. *Science* 341, 403–406 (2013). [PubMed: 23845944]
36. Suzuki J, Imanishi E & Nagata S Exposure of phosphatidylserine by Xk-related protein family members during apoptosis. *J. Biol. Chem* 289, 30257–30267 (2014). [PubMed: 25231987]
37. Petrova PSet al. TTI-621 (SIRP α .Fc): a CD47-blocking innate immune checkpoint inhibitor with broad antitumor activity and minimal erythrocyte binding. *Clin. Cancer Res* 23, 1068–1079 (2017). [PubMed: 27856600]
38. Barclay AN & van den Berg TK The interaction between signal regulatory protein alpha (SIRP α) and CD47: structure, function, and therapeutic target. *Annu. Rev. Immunol* 32, 25–50 (2014). [PubMed: 24215318]
39. Gagnon E, Schubert DA, Gordo S, Chu HH & Wucherpfennig KW Local changes in lipid environment of TCR microclusters regulate membrane binding by the CD3 ϵ cytoplasmic domain. *J. Exp. Med* 209, 2423–2439 (2012). [PubMed: 23166358]
40. Elliott JI et al. Phosphatidylserine exposure in B lymphocytes: a role for lipid packing. *Blood* 108, 1611–1617 (2006). [PubMed: 16684961]
41. Elliott JI et al. Membrane phosphatidylserine distribution as a non-apoptotic signalling mechanism in lymphocytes. *Nat. Cell Biol* 7, 808–816 (2005). [PubMed: 16025105]
42. Raghupathy Ret al. Transbilayer lipid interactions mediate nanoclustering of lipid-anchored proteins. *Cell* 161, 581–594 (2015). [PubMed: 25910209]
43. Andersen JP et al. P4-ATPases as phospholipid flippases—structure, function, and enigmas. *Front. Physiol* 7, 275 (2016). [PubMed: 27458383]
44. Van Blitterswijk WJ & Verheij M Anticancer mechanisms and clinical application of alkylphospholipids. *Biochim. Biophys. Acta* 1831, 663–674 (2013). [PubMed: 23137567]
45. Moreno-Smith Met al. ATP11B mediates platinum resistance in ovarian cancer. *J. Clin. Invest* 123, 2119–2130 (2013). [PubMed: 23585472]
46. Advani Ret al. CD47 blockade by Hu5F9-G4 and rituximab in non-Hodgkin’s lymphoma. *N. Engl. J. Med* 379, 1711–1721 (2018). [PubMed: 30380386]
47. WHO Classification of Tumours of Haematopoietic and Lymphoid Tissues Vol. 2 (eds Swerdlow SH et al.) Ch. 10 (IARC Press, 2008).
48. Ennishi Det al. Genetic profiling of MYC and BCL2 in diffuse large B-cell lymphoma determines cell-of-origin-specific clinical impact. *Blood* 129, 2760–2770 (2017). [PubMed: 28351934]
49. Ennishi Det al. Double-hit gene expression signature defines a distinct subgroup of germinal center B-cell-like diffuse large B-cell lymphoma. *J. Clin. Oncol* 37, 190–201 (2019). [PubMed: 30523716]

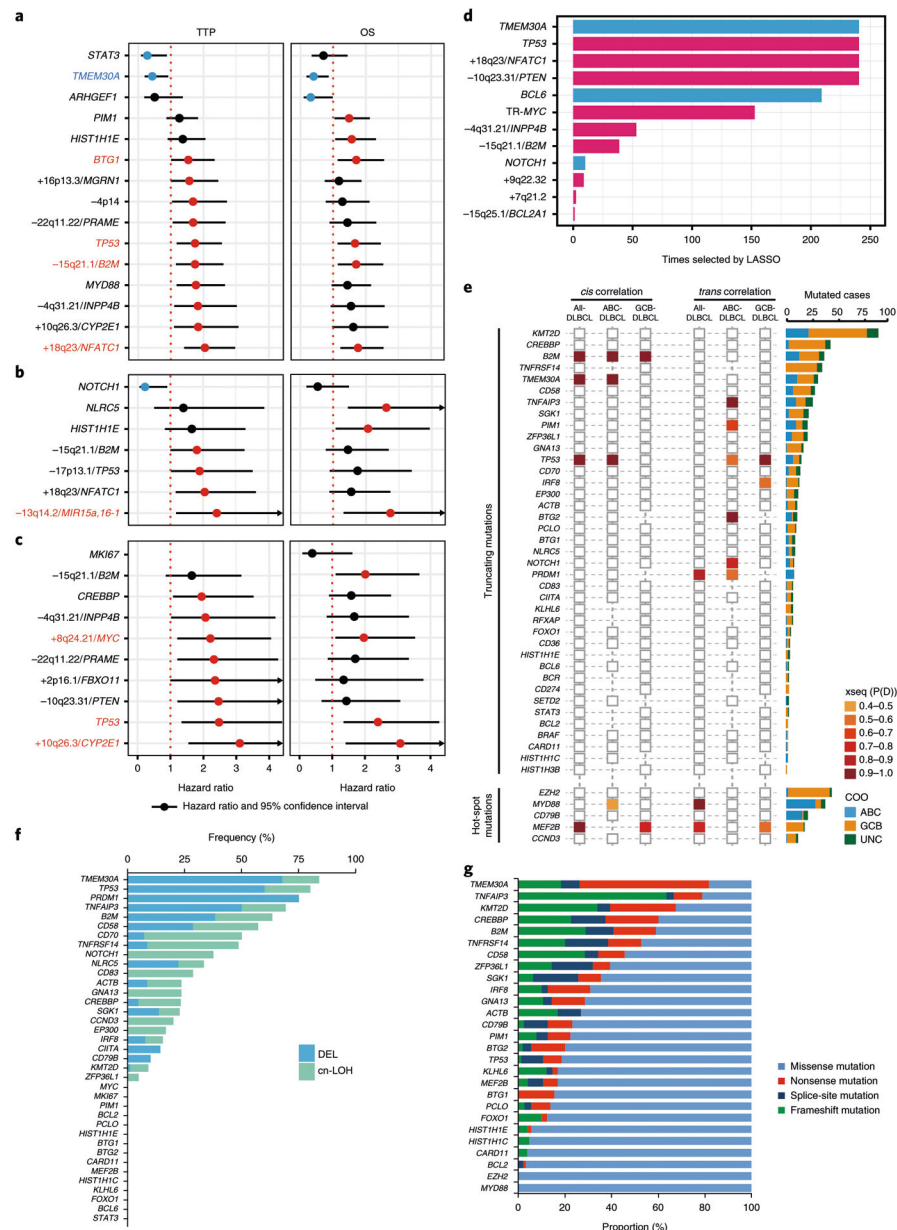


Fig. 1 | Impact of genetic alterations on prognosis and gene expression in DLBCL. **a,b,c**, Forest plots summarize the results of univariate analyses (TTP and OS) for mutated genes and representative copy-number alterations (CNAs) within GISTIC regions, which are significantly associated with prognosis (unadjusted P value < 0.05), in all-DLBCL ($n = 347$) (**a**), in ABC-DLBCL ($n = 104$) (**b**) and GCB-DLBCL ($n = 183$) (**c**). Hazard ratios and 95% confidence intervals are shown. Colored circles represent significant hazard ratios, and colored genes are significantly associated with both TTP and OS (blue, favorably prognostic; red, unfavorably prognostic). **d**, Frequency of selection of the genetic feature by the Cox-lasso predictive models generated in 238 iterations of leave-one-out cross validation. COO and IPI are included as control variables in all models. The bar plot (blue, favorable outcome; red, unfavorable outcome) shows the genes repeatedly selected in the

238 models. **e**, xseq-derived *cis* and *trans* effects of loss-of-function and hotspot mutations in all DLBCL tumors and each COO subtype (left). P(D) represents the probability that a recurrently mutated gene influences gene expression across the population of patients. A larger P(D) value represents a stronger inferred effect. Histogram (right) shows the number of each mutation in COO subtypes. **f**, Frequencies of occurrence of hemizygous deletion or copy-neutral loss of heterozygosity (cnLOH) in the loss-of-function mutated tumors. **g**, Proportions of mutation type in recurrently mutated genes. Mutated genes with frequency >10% are depicted.

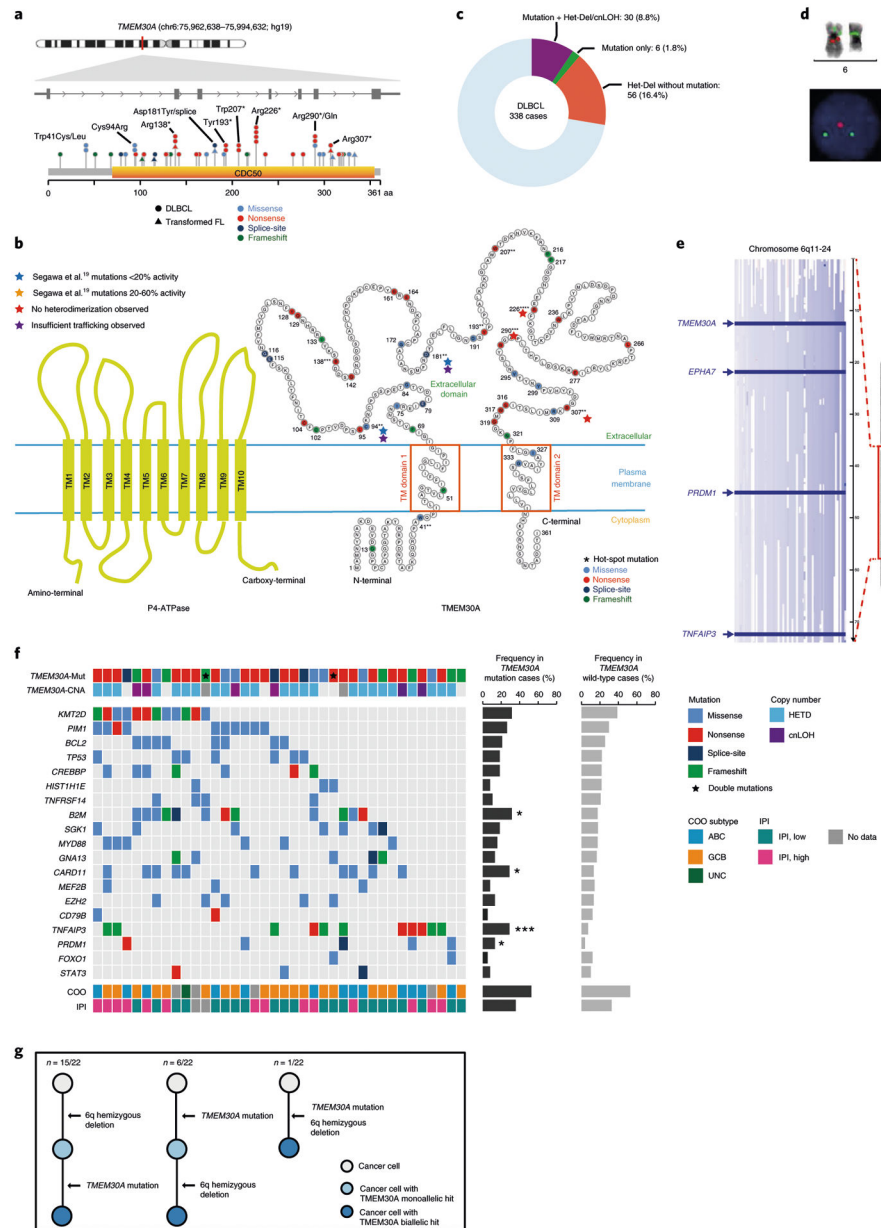


Fig. 2 | Genetic characterization of *TMEM30A*.

a, *TMEM30A* protein domain and the locations of 42 mutations identified in this study, affecting 38 DLBCL tumors, as well as 5 mutations found in transformed follicular lymphoma (FL) samples in our previous study²⁰. Multiple mutations affecting the same position are annotated. **b**, Schematic structure of the P4-ATPase and *TMEM30A* subunits consisting of two membrane-spanning domains with a large extracellular loop; 95% of variants are localized to extracellular domains, which are required for assembly with P4-ATPase. Flippase activities are annotated with colored stars. **c**, Distribution of DLBCL tumors harboring *TMEM30A* mutations, heterozygous deletions (Het-Del), and cNLOH, *TMEM30A* mutation without CNAs and heterozygous deletion without mutations. **d**, Heterozygous deletions were validated using fluorescence in situ hybridization

(FISH) assays in all nine analyzed samples. Two-color FISH assays use a red probe interrogating *TMEM30A* and a green probe interrogating *PIMI* on the chromosomal 6p arm as a reference. **e**, SNP6.0 copy-number heat map illustrating broad deletions affecting *TMEM30A*, *EPHA7*, *PRDM1* and *TNFAIP3* locus (dense blue line and arrow) on chromosome 6q11-24 in representative DLBCL tumors. **f**, Distribution of recurrent mutations, COO subtypes and IPI groups in 38 *TMEM30A*-mutated DLBCL tumors (left). The header includes the status of *TMEM30A* mutation and CNAs. Histograms (right) show the frequency of each alteration within *TMEM30A* mutated (dark gray) and non-mutated tumors (light gray). Two-sided Fisher's exact test was used to compare these frequencies according to the two groups. * $P < 0.05$, *** $P < 0.001$. **g**, Evaluating the evolutionary timing of *TMEM30A* mutations and 6q deletions. Each column depicts an evolutionary timing scenario for *TMEM30A* mutations and 6q deletions.

Author Manuscript

Author Manuscript

Author Manuscript

Author Manuscript

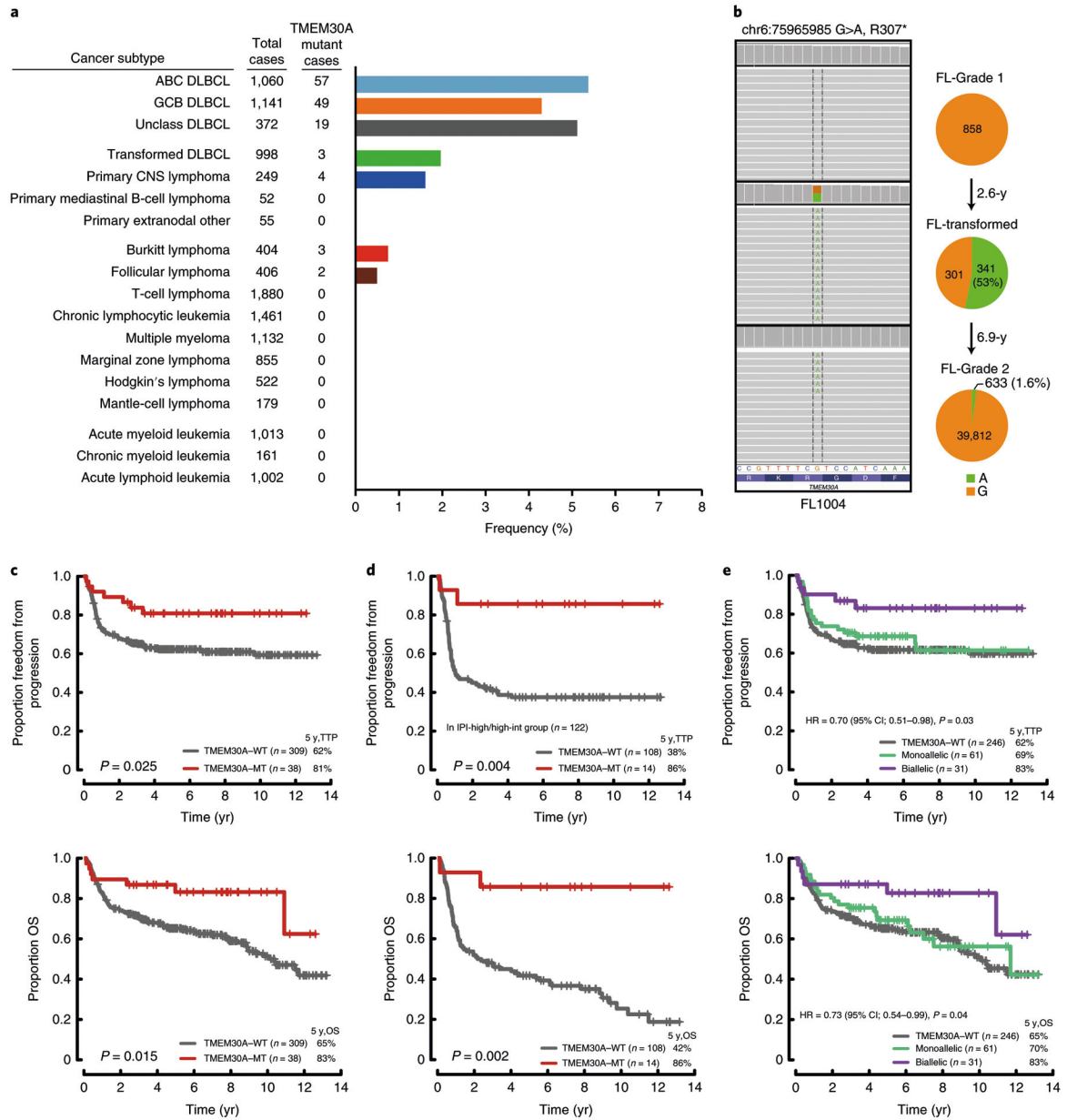


Fig. 3 |. Prevalence and clinical impact of *TMEM30A* mutation.

a, Bar plot showing the frequencies of *TMEM30A* mutation in lymphomas and other hematological malignancies, based on the previous literature and publicly available datasets.

b, Deep targeted sequence data of a representative transformed FL case (FL1004) for the affected position of the *TMEM30A* visualized in integrative genomics viewer (left) and variant allelic frequency visualized in pie chart (right), demonstrating the proportion of variant reads (variation indicated in green) at the time of diagnosis (FL-Grade 1), transformation (DLBCL) and relapse after transformation (FL-Grade 2). The time between initial diagnosis (FL-Grade1) and first relapse (FL-transformed) and between first relapse and second relapse (FL-Grade 2) is shown in years (y). **c-e**, Kaplan–Meier curves represent TTP (top) and OS (bottom) according to *TMEM30A* mutation in all DLBCL (**c**), in IPI-

high/high-intermediate group (**d**) and according to *TMEM30A* genetic status in all DLBCL (**e**). *P* values were derived from two-sided log-rank test (**c,d**) and Cox proportional-hazards model (**e**).

Author Manuscript

Author Manuscript

Author Manuscript

Author Manuscript

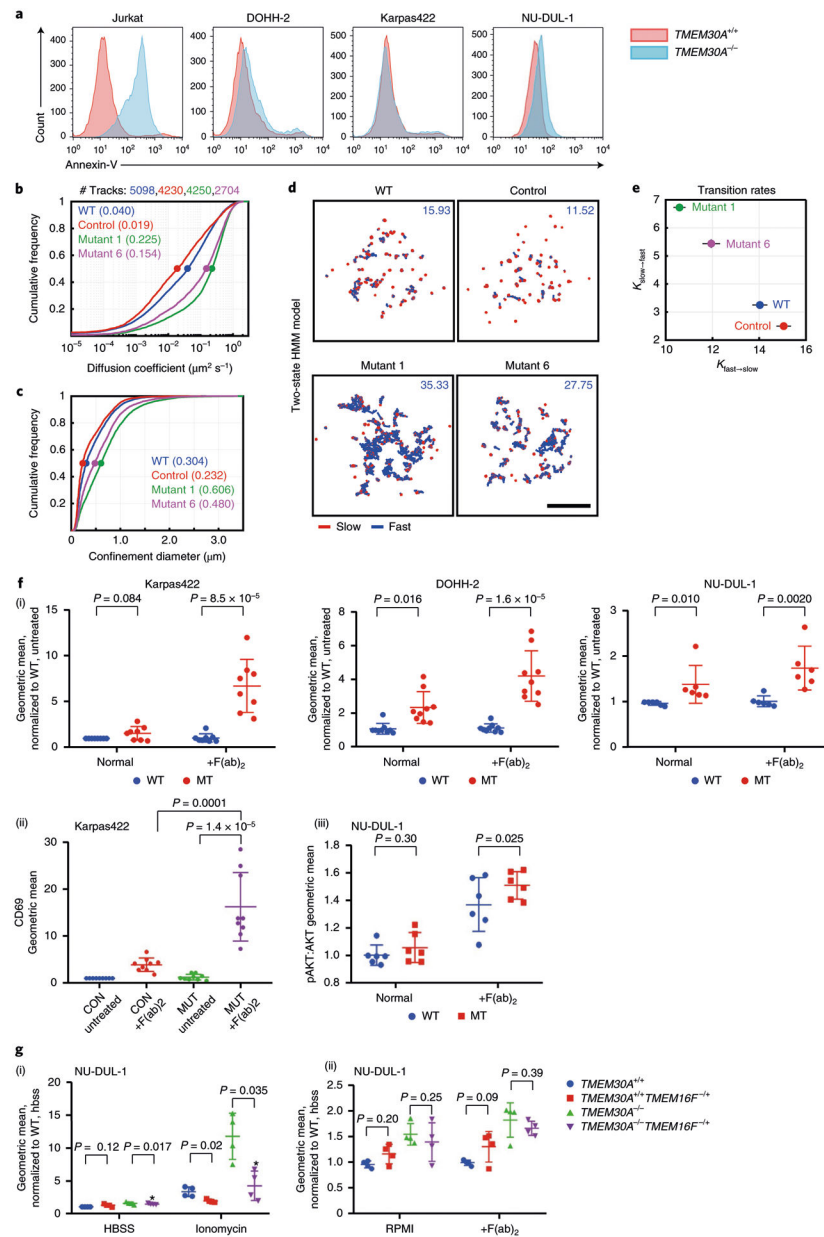


Fig. 4 | BCR mobility and B-cell signaling is increased in B-cell lymphoma lines with *TMEM30A* loss-of-function mutation.

a, Abundance of externalized PS was measured through flow cytometry by annexin V-APC binding in Jurkat, DOHH-2, Karpas422 and NU-DUL-1 under optimal growth conditions, comparing wild type (red) and *TMEM30A*^{-/-} (blue). **b–e**, BCR mobility and clustering in Karpas422 as measured by single-particle tracking analysis. All experiments were repeated independently three times with similar results. **b**, Cells were labeled with anti-IgG Fab–Cy3, settled onto poly-L-lysine-coated coverslips and imaged for 10 s at 33 Hz by total internal reflection microscopy. A representative experiment with Karpas422 is shown here. Single-state diffusion coefficients were calculated for all tracks, and cumulative frequency curves are shown. The dots on the curves indicate the median values and are reported in brackets. The total numbers of tracks analyzed were 5,098 (wild type), 4,230 (control), 4,250 (mutant

1) and 2,704 (mutant 6). **c**, The cumulative frequency curves of the confinement diameters with the median values (dots on the curves) indicated in brackets. **d**, BCR tracks were analyzed using a two-state HMM model to subdivide trajectories into slow-diffusing (red) and fast-diffusing (blue) segments, with dynamic transitions between these two inferred behaviors. Depicted are representative static trajectories of IgG BCRs that were segmented into inferred slow and fast states. The fraction of fast states from all tracks is indicated in blue. Scale bar, 5 μm . **e**, The transition rates ($K_{\text{slow} \rightarrow \text{fast}}$, $K_{\text{fast} \rightarrow \text{slow}}$) between the two states are shown. The dots indicate median values; lines indicate 95% confidence intervals ($n = 3$). **f**, Effects of overnight antigen stimulation by F(ab)₂ fragments on (i) PS exposure in *TMEM30A*^{-/-} and wild-type control cells, measured by annexin V-APC binding, (ii) induction of surface markers CD69 (Karpas422) and (iii) phosphorylation of AKT (NU-DUL-1), measured by flow cytometry. Graphs represent mean values \pm s.d. ((i) $n = 8$ (Karpas422), $n = 9$ (DOHH-2), $n = 6$ (NU-DUL-1), (ii) $n = 9$ and (iii) $n = 6$). All *P* values are based on an unpaired two-tailed Student's *t*-test. **g**, Alterations in PS externalization following (i) ionomycin and (ii) F(ab)₂ fragment stimulation following TMEM16F knockdown in NU-DUL-1 wild-type and *TMEM30A*^{-/-} cells. Graphs represent mean values \pm s.d. ($n = 6$). All *P* values are based on an unpaired two-tailed Student's *t*-test.

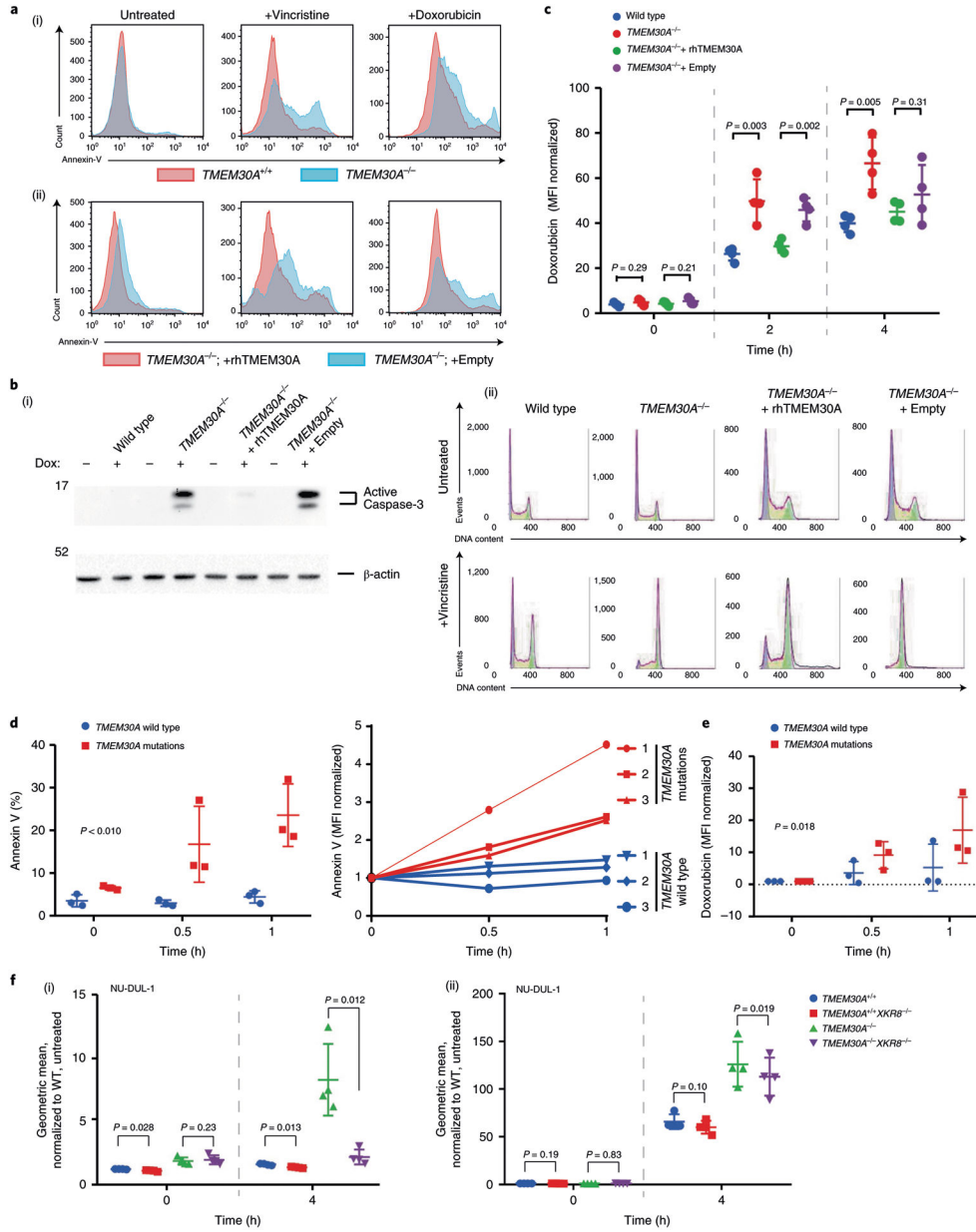


Fig. 5 | TMEM30A loss of function mediated increased drug uptake in DLBCL.

a, Effects of vincristine and doxorubicin, both components of the R-CHOP regimen, on PS exposure in Karpas422 *TMEM30A*^{-/-} and wild-type control. The top panel (i) compares wild-type (red) and *TMEM30A*^{-/-} (blue) events counted by flow cytometry. The lower panel (ii) compares *TMEM30A*^{-/-} expressing recombinant TMEM30A (rhTMEM30A, red) and a transformation empty-vector control (Empty, blue). **b**, Increased apoptotic signaling following incubation with doxorubicin as measurable by caspase-3 activation by western blot analysis (i), and vincristine, as measurable by a G2/M block through flow cytometry (ii), was compared in Karpas422 *TMEM30A*^{-/-}, wild type and *TMEM30A* transformants. Cropped images from the same western blot are shown. β -actin is used as a loading control. See Source Data Fig. 5. Experiments were repeated independently three times with similar

results. **c**, Doxorubicin uptake in Karpas422 *TMEM30A*^{-/-}, wild type and *TMEM30A* transformants over time was detected by flow cytometry. Graphs represent mean values ± s.d. ($n = 4$). All *P* values are based on an unpaired two-tailed Student's *t*-test. **d**, Externalized PS following increasing doxorubicin incubation times was measured in gated B-cells from DLBCL patient tumor biopsies expressing normal or *TMEM30A*-null (summary bar plot, left; movement of each sample, right). Graphs represent mean values ± s.d. ($n = 3$). *P* value is based on a two-way ANOVA test. **e**, Doxorubicin uptake in gated B-cells from DLBCL patient tumor biopsies was measured over time by flow cytometry. Graphs represent mean values ± s.d. ($n = 3$). *P* value is based on a two-way ANOVA test. **f**, Alterations in PS externalization (i) and doxorubicin (ii) uptake including XKR8 knockout in NU-DUL-1 wild type (WT) and *TMEM30A*^{-/-} cells over time.

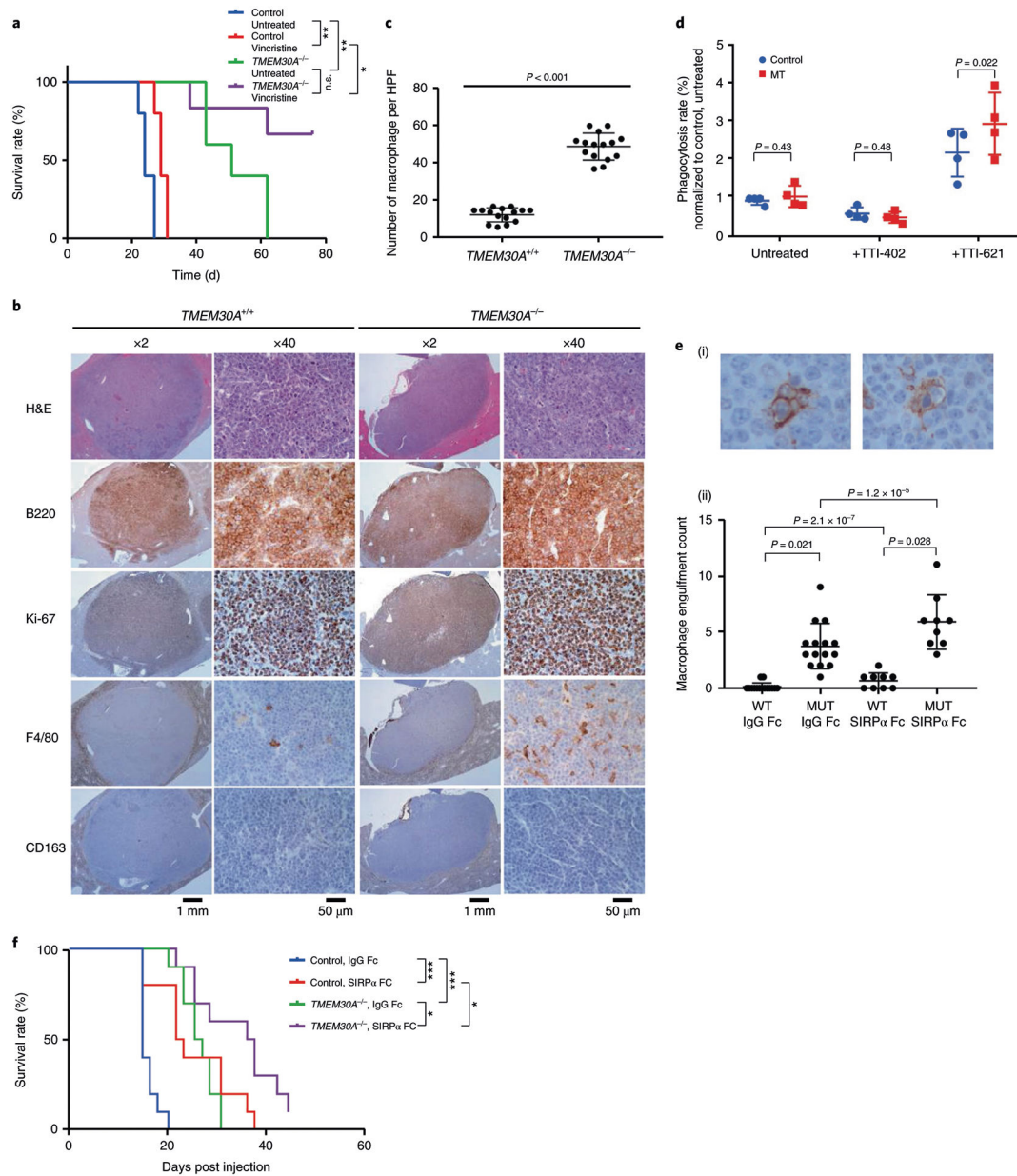


Fig. 6 | TMEM30A loss of function enhanced survival with treatment and increased macrophage infiltration in mouse models.

a, Xenotransplantation models of DOHH-2 cells with wild-type or *TMEM30A*^{-/-} subcutaneously injected into NSG mice (5 per group). Vincristine treatment (0.1 mg kg⁻¹) or saline control (untreated) was administered when tumor volumes per group reached 100 mm³. Kaplan–Meier plots showing overall survival of NSG xenograft mice. *P* value is based on a Mantel–Cox test. **P* < 0.05, ***P* < 0.01. **b**, Liver tissues from A20 wild-type *Tmem30a* or *Tmem30a*^{-/-} syngeneic mouse models (*n* = 5 mice per group), sacked within first palpable presentation of tumor growth (‘early sac’, ~day 20), were stained with hematoxylin and eosin (H&E), B220, Ki-67, F4/80 and CD163. **c**, Macrophage count comparison per tissue within 3 randomly selected $\times 400$ high-power field (HPF) regions per tumor from 5 separate mice per group with early sac (A20 model). *P* value is based

on an unpaired two-tailed Student's *t*-test. **d**, In vitro macrophage engulfment assays of wild-type or *TMEM30A*^{-/-} DOHH-2. Cells were pretreated with 1 μM TTI-621 or TTI-402 preceding coculture with macrophages. The phagocytic index was measured by flow cytometry. Graphs represent mean values ± s.d. (*n* = 4). All *P* values are based on a paired two-tailed Student's *t*-test. **e,f**, Xenotransplantation models of DOHH-2 cells with wild-type or *TMEM30A*^{-/-} subcutaneously injected into NSG mice (*n* = 10 mice per group). TTI-621 treatment (10 mg per kg body weight) or TTI-402 (6.67 mg per kg body weight) was initiated when tumor volumes per group reached 100 mm³. Kaplan–Meier plots showing overall survival of NSG xenograft mice. **e**, Visualization and quantitation of engulfed B cells in macrophages as detected by CD68 antibody with H&E counter staining. Two representative images of engulfment from TTI-621 treated *TMEM30A*^{-/-} group (i). Macrophage engulfment counts from each mouse model treatment group (ii). Graphs represent mean values ± s.d. (*n* = 15 (control), *n* = 9 (mutant)). All *P* values are based on a paired two-tailed Student's *t*-test. **f**, Kaplan–Meier plots showing overall survival of NSG xenograft mice. *P* value is based on a Mantel–Cox test. **P* < 0.05, ****P* < 0.001; n.s., not significant.